Electrochemically driven Mechanical Energy Harvesting

by

Sangtae Kim

Submitted to the Department of Materials Science and Engineering
in partial fulfillment of the requirements for the degree of

Doctor of Philosophy in Materials Science and Engineering

at the

MASSACHUSETTS INSTITUTE OF TECHNOLOGY

June 2016

Signature redacted

Author .....
Department of Materials Science and Engineering
May 18, 2016

Signature redacted

Certified by...
Ju Li
Battelle Energy Alliance Professor of Nuclear Science and Engineering
Professor of Materials Science and Engineering
Thesis Supervisor

Signature redacted

Accepted by ....
Donald Sadoway
Chair, Departmental Committee on Graduate Students

Electrochemically driven Mechanical Energy Harvesting

by

Sangtae Kim

Submitted to the Department of Materials Science and Engineering
on May 18, 2016, in partial fulfillment of the
requirements for the degree of
Doctor of Philosophy in Materials Science and Engineering

Abstract

Efficient mechanical energy harvesters enable various wearable devices and may also act as auxiliary energy supply to isolated area. In this thesis, I present a novel class of mechanical energy harvesters based on stress-voltage coupling in electrochemically alloyed electrodes. The device consists of two identical Li-alloyed Si as electrodes, separated by electrolyte-soaked polymer membranes. Bending-induced asymmetric stresses generate chemical potential difference, driving lithium ion flux from the compressed to the tensed electrode to generate electric current. Unbending the device reverses the ion flux, generating electrical current in the opposite direction. The thermodynamic analyses reveal that the ideal energy-harvesting efficiency of this device is dictated by the Poisson's ratio of the electrodes. For the thin-film-based energy harvester used in this study, the device has achieved the overall efficiency of 0.6% and a generating capacity of 15%.

The device also presents unique characteristics over the existing type of mechanical energy harvesters. Compared to piezoelectric or triboelectric generators, the prototype demonstrates low internal impedance of the order of 300Ω as opposed to 100MΩ in the other two types, and continuous electric current of the order of 3 seconds as opposed to 50ms in the other two types.

From kinetics analysis, we show that the device's electric current generation is limited by lithium diffusion inside the Li_xSi electrode for sufficiently thick electrodes and by electrolyte diffusion for thin electrodes below 400nm. Tuning the current peak widths between 5s and 22s was demonstrated experimentally. The framework developed in the kinetics analyses also suggests that the device may be used as a spectroscopic tool to measure lithium diffusivity inside electrochemical alloys. The experimentally observed kinetics suggests lithium diffusivity on the order of $10^{-10}cm^2/s$ in $Li_{3.1}Si$.

The device demonstrates a practical use of stress-composition coupling in electochemically active alloys to harvest low-grade mechanical energies from various low-frequency motions, such as everyday human activities. The analyses present the quantitative strategies to optimize the device in terms of its total energy output, kinetic behavior and ultimately the design principles for an energy harvester optimized

for harvesting a specifically targeted frequency motion.

Thesis Supervisor: Ju Li
Title: Battelle Energy Alliance Professor of Nuclear Science and Engineering Professor of Materials Science and Engineering

Acknowledgments

I would like to express my deep gratitude to my thesis committee members, Prof. Carl Thompson and Prof. Jeff Grossman. Their insights and willingness to provide help opened up various intriguing perspectives as well as guiding me in providing accurate scientific descriptions of my research. I appreciate their time in evaluating this thesis and their encouragements.

I would like to thank my thesis advisor, Professor Ju Li. I learned from his creativity and insights in materials science. He has been a patient advisor, warm-hearted mentor and passionate role-model. Without his emotional support as well as intellectual guidance, this thesis would not have been possible. I deeply enjoyed interacting with him, being part of his research group and learning from the numerous opportunities he provided me with. I was allowed to experience projects from various disciplines of materials science and this made this interdisciplinary work possible. I learned to become a researcher under his steady and personal guidance and will continue to learn from this experience.

I acknowledge the experimental facilities and the staff at Center for Materials Science and Engineering (CMSE) at MIT and Center for Nanoscale Systems (CNS) at Harvard University. The publicly available facilities provided essential tools and apparatus to build experimental foundations of this work. Dr. Shiahn Chen and Dr Yong Zhang from CMSE are graciously acknowledged for their help and training for electron microscopy facilities. I appreciate Dr. Jiangdong Deng, Dr. Edward Macomber and Mr. Mac Hathaway from CNS for their detailed training and guidance with my experimental work.

Each and every member of Li group has been of great fun, inspiration and motivation. I would especially like to thank Liang Qi, Xiaofeng Qian, Kejie Zhao, Wenbin Li, Yang Yang, Sina Ardakani, Soon Ju Choi, Kangpyo So, Cong Su and Ziqiang Wang for the wonderful memories in the office together.

I would like to thank friends who supported me emotionally. Members of Boston 3040 tennis club have been my emotional resort at all times of trouble, and I will never

forget the funs we had every Saturday evening. Members of First Korean Church in Cambridge are true friends who helped me develop my religious belief. Every member in Korean Graduate Student Association and Department of Materials Science and Engineering remain to be acknowledged for their company and joy.

Lastly, I would like to thank my family for their patience, support and endless love towards me. For fourteen years of studying abroad, they have always been there for me every possible way.

Contents

List of Figures

List of Tables

Chapter 1

Introduction

Efficient energy-harvesting devices, which convert energies otherwise wasted to electricity, help decentralize power generation and reduce the distance of electricity transmission. Over the last few decade, several types of mechanical energy harvesters including piezoelectric generators have been demonstrated and improved in energy generation capability.[1–3] Nevertheless, their volumetric energy density and efficiency have yet limited their applications and commercialization. The effort to developing better mechanical energy harvesters has in large part been limited by the materials. For the case of piezoelectric generators, the existing materials' piezoelectric coefficients have a limited range among materials available to us.[4] In this thesis, I introduce a novel type of mechanical energy harvester based on electrochemical alloys and investigate the involved materials science with respect to the thermodynamics, kinetics and mechanics perspective. This chapter begins with a brief introduction of conventional mechanical energy harvesters (Section 1.1) and electrochemical alloys (Section 1.2). The chapter ends with the motivation and an overview of the thesis (Section 1.3).

1.1 Mechanical energy harvesters

Mechanical energy harvesters are a class of devices that convert many forms of mechanical energy directly into electricity. In large, the existing forms of such de-

vices include piezoelectric generators[1], triboelectric generators [3]and electrokinetic generators.[2, 5, 6] They are in most cases less efficient than turbines and target small scale energy scavenging. One such application is harvesting mechanical energy from everyday human motions such as walking. Force exerted by human motions are often not sufficient in terms of geometrical factors, applied stress and motion frequency for turbine operation.

1.1.1 Piezoelectric generators

Piezoelectric generators convert mechanical strain into electricity via dipole moment created when a crystalline material is strained. When the material is strained in a certain crystallographic direction, the ions inside the material respond differently in terms of direction and extent such that the crystal symmetry gets broken. With the broken symmetry, dipole moment is induced between displaced cations and anions in the unit cell, creating an electric potential difference and current output. A well-known piezoelectric material is lead zirconate titanate ($Pb[Zr_xTi_{1-x}]O_3$) in perovskite crystalline structure. (Figure 1-1) When the material is strained in <001> direction, titanium cation (Ti^{4+}) migrates more towards the direction of strain than the surrounding oxygen anions, creating a polarization in the direction of strain. This polarization results in net electric potential. Figure 1-2 illustrates the electric current output of a typical piezoelectric generator. The ratio between induced polarization and applied strain in a specific crystallographic direction is called piezoelectric coefficients, d_{xy}, with x and y denoting the directions of polarization and applied stress, respectively. This is a fundamental materials property. Fig. 1-2 illustrates the short circuit current density for a typical bending-type piezoelectric generators.

Since piezoelectric effect relies on spontaneous symmetry breaking on strained crystals, randomly distributed polycrystalline crystals do not exhibit net piezoelectric effect. Thus, textured polycrystalline crystals has been used in most piezoelectric generators, and synthesis of such crsytals have been studied extensively.[7] The highest piezoelectricity is thus expected from single crystalline bulk materials with highest piezoelectric constants. One such material is single crystalline PMN-PT

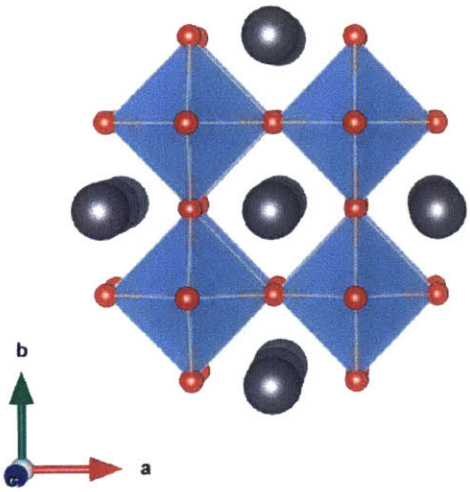

Figure 1-1: $PbTiO_3$ perovskite crystal structure. Light blue, grey and red spheres indicate Ti, Pb and O, respectively.

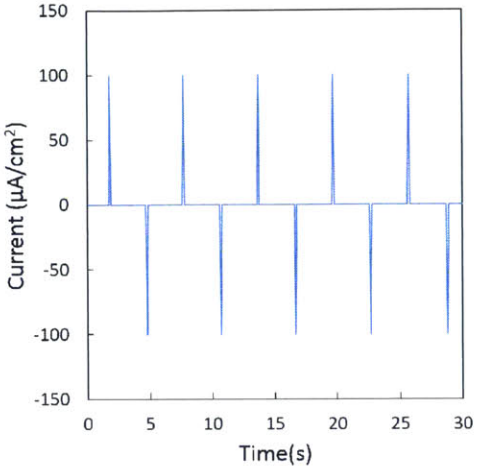

Figure 1-2: Typical current output of a piezoelectric thin film generator. Bending creates a positive peak and unbending a negative peak.

$(0.72Pb(Mg_{1/3}Nb_{2/3})O_3\text{-}0.28PbTiO_3)$. The bending type generator based on single crystalline thin film on flexible substrate has been fabricated and demonstrated.[8]

1.1.2 Triboelectric generators

Triboelectric generators operate by the contact electrification between two surfaces of different tribo-polarity. When a mechanical stress forces two surfaces separated by a small distance touch each other, charge transfer at the surface occurs, polarizing the surfaces. This spontaneous polartization results in electric current when the two electrodes are connected via external circuit. As the force gets removed, the polarized surfaces induce electric field between the two and these charges migrate to neutralize the electrodes, generating electric current in the opposite direction. Similar to the piezoelectric generators, repeated stress and stress-free states result in alternating voltage and current output.

Several geometries and electrode material combinations have been investigated to optimize this type of generator. For instance, various geometries between the two electrodes involving contact mode[9], sliding mode[10] and free standing modes have

been investigated[11]. Typical choice of electrode materials includes polyamide (Nylon), polyvinylidene fluoride (PVDF), polytetrafl uoroethylene (PTFE), polyimide (kapton) and aluminum. The detailed quantification of these materials' surface triboelectrification property and thus the justification of electrode choices remain to be investigated.

This type is claimed to involve distinct advantage on low fabrication cost based on polymeric electrode materials. The use of polymeric materials, on the other hand, also involves high internal resistance of the electrode materials. This is manifested by the high voltage output on the order of 100V and low current output (10μA).[12] Experiments with connected external loads suggest that the optimum energy output is delivered approximately when 10MΩ is connected to the generator.[11] Assuming simple circuit geometry, this indicates that the internal resistance, arising from polymeric electrodes is on the order of 10MΩ.

1.1.3 Electrokinetic and other generators

Electrokinetic generators operate by mechanically modulating electric double layer and may involve a variety of forms. In one form, a salty water droplet is sandwiched between two conducting plates with different contact area.[6] The interfaces between water and plates develop electrical double layer with certain capacitance. When the plate-droplet sandwich is pressed, the electrical double layers are disturbed, redistributing charge inside the droplet and on surface. When the two plates are connected, the two plates exchange charge, adjusting to the mechanically modulated electric double layer capacitance.[2, 5] Another form involves similar principle. The surfaces of capillary containing an electrolyte solution develops surface charge via adsorption or ion dissolution. These surface charges repel co-ions while attracting opposite-charged ions. This creates a net ionic current under concentration gradient.

1.2 Stress effects on electrochemical alloys

In this section, electrochemical alloys and the effect of stress on the alloying kinetics will be introduced briefly. The alloys feature unique characteristics in terms of microstructure control, controlled alloy kinetics and strong bidirectional coupling between stress and alloying kinetics.

1.2.1 Electrochemical alloys

Electrochemical alloys are metallic compounds formed via electrochemical insertion or deposition from ionic species. Formation via electrochemical means often allows precise control of the composition and microstructure without the need for extensive heat or pressure treatment. For instance, microstructural controls such as atomic layer deposition[13], nucleation of twin boundaries[14], or epitaxial heterogeneous structures have been demonstrated via electrodeposition.[15] In the context of lithium ion battery electrodes, the potential at which crystalline phase nucleates has been characterized by detailed X-ray diffraction studies.[16] This enables the synthesis of single phase lithium silicon alloy with potential cut-off.

These alloys are also characterized by their ability to change composition when relevant electrochemical potentials are applied. For example, lithium alloys made by such means have drawn extensive research interest as lithium ion battery electrode, based on their ability to accept a large amount of lithium.[17] Examples for such materials include lithium silicide (Li_xSi)[18], or lithium germanide (Li_xGe)[19]. These compounds accept up to 4.4 moles of lithium per mole of host material (Si or Ge), a significantly larger amount than conventional intercalation compounds such as lithiated graphite (Li_xC_6) or Li_xCoO_2. The alloys differ from the intercalation compounds such that they may be amorphous as well as crystalline, undergo structural evolution with lithium insertion or extraction and do not have defined 1D, 2D or 3D diffusion channel.

1.2.2 Lithiation induced stress

Insertion or removal of lithium involves a finite amount of volume change, since lithium atoms carry a small amount of volume. In the small insertion/removal limit, this volume change can be expressed in terms of chemical strain.

$$\epsilon_{\text{chemical}} = \frac{N_{\text{Li}}\Omega_{\text{Li}}}{V_{\text{electrode}}} \tag{1.2.1}$$

Here, N_{Li}, Ω_{Li} and V_{alloy} refer to the number of lithium atoms transported, volume occupied by a single lithium atom inside the alloy and total volume of the alloy, respectively. The chemical strain can be assumed to be hydrostatic since small volume expansion by lithium insertion is expected in all directions. In the small strain and elastic limit, hydrostatic stress equivalent to the product of hydrostatic strain and bulk modulus builds up.

In battery applications, large amount of lithium transfer is expected. In $Li_{4.4}Si$, volume expansion up to 300% has been reported.[20] Often in this case, the strain exceeds elastic limit and the material has been reported to plastically flow.[21, 22] In the plastic flow region, stress remains almost unchanged with increasing strain. Similar behavior has been observed for both insertion and extraction induced stresses, although anisotropy between the two has been observed.[23] Large amount of lithium insertion or extraction often involve two phase behavior - the lithiated and unlithiated phases. Since lithiation is a gradual process, stress builds up on the phase boundary between the lithiated and unlithiated phases as well.[24]

1.2.3 Stress effects on alloying kinetics

Both lithiation induced stress and external stress are known to affect the alloying kinetics. For instance, stress is known to mediate the lithiation kinetics; faster lithiation on less stressed region than that on the more stressed region has been reported.[25] During the lithiation of bent germanium nanowires, lithiation was observed to occur on the tensed region first, then propagating to the compressed region. This evidences

the notion that lithiation gets slowed down inside the core of a spherical particle, since lithiated phase places compressive stress on the unlithiated core and phase boundary.[24, 26, 27]

Also, anisotropy in alloying kinetics on different crystalline planes has also been reported. In single crystalline silicon pillars, strong anisotropy in lithiation kinetics depending on the crystalline orientation has been reported.[28] A significant amount of swelling in (110) family of crystalline planes has been observed while there was minimum swelling in (111) family of planes. This indicates fast insertion kinetics in (110) planes as opposed to slow kinetics in (111) planes. This strong anisotropy in kinetics often induces large amount of stress on lithiated outer surface, leading to surface fracture.[29] This anisotropy in insertion kinetics also depends strongly on the alloy matrix. For instance in germanium alloys, isotropic swelling has been reported during the lithiation of crystalline germanium particles, indicating isotropic insertion kinetics.[30] Higher fracture resistance has been reported for lithiated germanium particles than that of lithiated silicon particles.

1.2.4 Strong coupling between stress and insertion kinetics

Strong coupling and bidirectional effect between stress and insertion kinetics has been manifested during electrochemical alloying of lithium.[22, 25] For instance, lithium insertion generates stress inside the electrode by carrying a finite amount of volume and strain. On the other hand, the generated stress balances the insertion kinetics such that insertion favors less-compressed regions. Lithiation, in turn, mediates the effect of stress on the electrode, such as pore formation, defect nucleation or degradation of the electrode. This effect can be understood in terms of viscoelastic properties of the electrodes. Nabarro-Herring creep demonstrated that stress inside materials can be mediated by the atomic motion inside the material via bulk diffusion.[31] Noting that the electrochemical alloys are capable of adjusting their compositions depending on the electrochemical potential, active insertion or extraction of lithium may occur to mediate the stresses present inside the alloy. When the stress exceeds a threshold for such mediation, anomalies such as pore formation or defect nucleation are expected

to happen.

1.3 Motivations and Overview

The need for efficient mechanical energy harvesters has been increasing with the rising interest in clean energy technology. The application of piezoelectric devices in small scales has been used for long, including electric cigarette lighter or portable spark generators. Nevertheless, large-scale applications in energy harvesting or generation have recently been attempted. A British start-up company Pavegen, inc. developed a road pavement tile that lights up a streetlamp when stepped upon by passengers. An Israeli start-up company Innowattech demonstrated a smart highway with piezoelectric generators built underneath the highway, providing electricity to road signs and local energy grid. California state government considered employing smart highway to all of its state highways and published a report on its economic viability.[32] With the advent of wearable devices and internet of things (IoT), the need for efficient mechanical energy harvesters is anticipated to grow.

While the above-mentioned conventional energy harvesters possess certain advantages and improvements in power density, several fundamental limitations exist in these types. For instance, the electric currents generated by piezoelectric and triboelectric generators last for a very short amount of time, on the order of 50msec. This feature owes to the fundamental mechanisms of these generators, which are either dipole moment switching in ceramic crystals or triboelectric induction. Under a constant load, the devices are capable of generating current that lasts for a very short moment. For this reason, the total amount of charge generated is small, unless the mechanical stress input acting on the generator is constantly switched in direction. These generators are thus best suited for vibration harvesting for vibrations over 20Hz, notably higher than that of everyday human motions. While the use of clamped resonators[33] or springs[34] transforms low frequency motions into vibrations of the resonators, it constrains the geometry and size of the devices.

Secondly, the conventional piezoelectric or triboelectric generators have notably

high internal resistance on the order of 1-100MΩ. Internal resistance is a measure of energy dissipation when the generated electricity powers the external loads, an important index characterizing energy utilization efficiency of a device. Such high impedance indicates that that a majority of the generated electricity gets dissipated as heat to the internal resistance. Also, many commercial applications of electricity, including charging a secondary batteries, has much lower impedance on the order of 100Ω, often not exceeding 1000Ω. The mismatch in impedance between the energy harvester and application results in significantly reduced efficiency, unless a complex circuitry matching the impedance is employed. Since the circuits consume power, the loss in efficiency as well as the difficulty in applying the generators in some applications including wearable devices are unavoidable.

Lastly, some of the piezoelectric and triboelectric generators have environmental concerns, when employed in large scale applications. Many of the successful piezoelectric generators contain lead in its core ceramic components. Lead is considered toxic in many countries including the United States and many parts of Europe. Especially in Europe, the use of lead has been discouraged by the restriction of hazardous substance directive (RoHS).[35] The toxicity also arises health concerns for wearable device applications. The use of polymeric materials in triboelectric generators also place concern for its disposal, since the polymers in the devices are not bio-degradable. The possibility of fatigue wear for these polymer surfaces has also been raised for long term applications.

In this thesis, I present our work on a novel class of mechanical energy harvester, guided by electrochemical principles and stress-voltage coupling in electrochemical alloys. The device overcomes some of the fundamental limitations mentioned above, including continuous electric current generation, low internal resistance and non-toxic, environmentally benign choice of materials. Considering the interdisciplinary nature of this work, we will begin the thesis by introducing the fundamental concepts and experimental techniques used in the work (Chapter 2). We will then introduce the electrochemically driven mechanical energy harvester in Chapter 3. The chapter will include thermodynamic analysis on the device's working principle as well as experi-

mental demonstration of a working prototype. The chapter will end by comparing the energy output of the device with well-known piezoelectric generators in similar device geometry. In chapter 4, I will outline the kinetic processes of the device, introducing the timescale tunability of this type of mechanical energy harvester. The following chapter will outline the electrode design principles considering the thermodynamic and kinetic analysis presented in the previous chapters. The thesis will end with relevant conclusion (chapter 6) and directions for future work (chapter 7).

Chapter 2

Fundamental concepts and experimental techniques

The work in this thesis involves fundamental concepts and experimental techniques from various disciplines including thermodynamics, kinetics, electrochemistry, solid mechanics and micro-nano fabrication. Therefore, we briefly outline the fundamental concepts, nomenclature, notations, derivations and experimental techniques in this chapter.

2.1 Thermodynamic potential and stress contribution

2.1.1 Stress and strain

Materials under externally applied force deforms over time by shape change, sometimes accompanied by a form of motion. In the language of solid mechanics, the position of material elements in the reference frame (t = 0) is illustrated by $\boldsymbol{X}$ and that in the material frame ($t = t_0$) by x. The mapping between the two frames can be expressed using the following notation.[36]

$$\mathrm{x} = \boldsymbol{\chi}(\boldsymbol{X}, t) \tag{2.1.1}$$

The deformation gradient $\boldsymbol{F}(\boldsymbol{X},t)$, a differential tensor quantity illustrating an infinitesimal deformation, can be expressed as the following:

$$\begin{aligned} \boldsymbol{F}(\boldsymbol{X},t) &= \frac{\partial \chi(\boldsymbol{X},t)}{\partial \boldsymbol{X}} \text{such that} \\ d\boldsymbol{x} &= \boldsymbol{F} d\boldsymbol{X} \end{aligned} \tag{2.1.2}$$

The displacement ($\boldsymbol{u}$) and displacement gradient ($\boldsymbol{H}$) can be expressed in terms of the mapping (χ) and deformation gradient($\boldsymbol{F}$), respectively.

$$\begin{aligned} \boldsymbol{u}(\boldsymbol{X},t) &= \chi(\boldsymbol{X},t) - \boldsymbol{X} \\ \boldsymbol{H}(\boldsymbol{X},t) &= \frac{\partial \boldsymbol{u}(\boldsymbol{X},t)}{\partial \boldsymbol{X}} = \boldsymbol{F}(\boldsymbol{X},t) - \boldsymbol{I} \end{aligned} \tag{2.1.3}$$

Noting that the deformation gradient contains both rigid body rotation and stretch components, the two can be separated by the polar decomposition theorem as the following:

$$\boldsymbol{F} = \boldsymbol{R}\boldsymbol{U} = \boldsymbol{V}\boldsymbol{R} \tag{2.1.4}$$

The rotation matrix $\boldsymbol{R}$, by definition, satisfies the following:

$$\boldsymbol{R}\boldsymbol{R}^{\top} = \boldsymbol{I} \tag{2.1.5}$$

The right and left stretch components, U and V, are symmetric tensors with the following definition in terms of deformation gradient:

$$\begin{aligned} \boldsymbol{U} &= \sqrt{\boldsymbol{F}^{\top}\boldsymbol{F}} \\ \boldsymbol{V} &= \sqrt{\boldsymbol{F}\boldsymbol{F}^{\top}} \end{aligned} \tag{2.1.6}$$

Based on these notations, strain tensor can be defined as the following.

$$\begin{aligned} \boldsymbol{E} &= \frac{\boldsymbol{F}^{\top}\boldsymbol{F}}{2} \\ \boldsymbol{E} &= \frac{(\boldsymbol{H} + \boldsymbol{H}^{\top} + \boldsymbol{H}^{\top}\boldsymbol{H})}{2} \\ \text{where} \quad \boldsymbol{H} &= \boldsymbol{F} - \boldsymbol{I} \end{aligned} \tag{2.1.7}$$

In the case of small displacement gradient $\boldsymbol{H}$, the second order term may be neglected to result in infinitesimal strain tensor.

$$\boldsymbol{\epsilon} = \frac{(\boldsymbol{H} + \boldsymbol{H}^{\top})}{2} \tag{2.1.8}$$

In cartesian coordinates, the symmetric tensor quantity can be expressed in terms of a matrix.

$$[\epsilon] = \begin{bmatrix} \epsilon_{11} & \epsilon_{12} & \epsilon_{13} \\ \epsilon_{21} & \epsilon_{22} & \epsilon_{23} \\ \epsilon_{31} & \epsilon_{32} & \epsilon_{33} \end{bmatrix} \quad \text{such that}$$
$$\epsilon_{11} = \frac{\partial u_1}{\partial \boldsymbol{X_1}}, \quad \epsilon_{12} = \epsilon_{21} = \frac{1}{2}\left[\frac{\partial u_1}{\partial \boldsymbol{X_2}} + \frac{\partial u_2}{\partial \boldsymbol{X_1}}\right] \tag{2.1.9}$$

The stress tensor is expressed in a similar formalism. The definition of stress derives from force acting on surfaces of material (=surface traction). Specifically,

$$\boldsymbol{t}(\boldsymbol{n}) = \boldsymbol{\sigma}\boldsymbol{n} \tag{2.1.10}$$

The balance of momentum requires that the stress tensor be symmetric. In other words, stress does not provide any net torque on the system.

$$\boldsymbol{\sigma} = \boldsymbol{\sigma}^{\top}, \quad \boldsymbol{\sigma}_{ij} = \boldsymbol{\sigma}_{ji} \tag{2.1.11}$$

In cartersian coordinates, the tensor can be expressed in terms of a matrix.

$$[\epsilon] = \begin{bmatrix} \sigma_{11} & \sigma_{12} & \sigma_{13} \\ \sigma_{21} & \sigma_{22} & \sigma_{23} \\ \sigma_{31} & \sigma_{32} & \sigma_{33} \end{bmatrix} \tag{2.1.12}$$

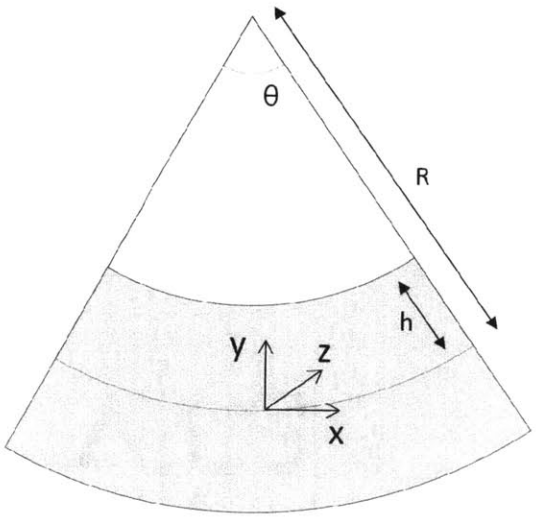

Figure 2-1: Bending geometry illustrated as a simple composite beam bending. The beam consists of three layers: bottom and top thin films sandwiching a middle layer

Stress can be decomposed into hydrostatic stress and deviatoric stress as the following:

$$\begin{aligned} \boldsymbol{\sigma} &= \boldsymbol{\sigma}_{\text{hydro}} + \boldsymbol{\sigma}_{\text{dev}} \\ \text{where} \quad \boldsymbol{\sigma}_{\text{hydro}} &= \frac{1}{3}(\text{tr}\boldsymbol{\sigma})\boldsymbol{I} \quad \text{and} \quad \boldsymbol{\sigma}_{\text{dev}} = \boldsymbol{\sigma} - \boldsymbol{\sigma}_{\text{hydro}} \end{aligned} \tag{2.1.13}$$

It is worth noting that the thermodynamic work done by stress is expressed as the following.[37]

$$dW = -V \sum_{ij} \sigma_{ij} d\epsilon_{ij} \tag{2.1.14}$$

Note that the sign convention where stress acting on a surface is given by $-\sigma_{ij}$. Often, the work done in gaseous systems is given by PdV, with isotropic gaseous pressure P.

2.1.2 Stress states in constrained thin film bending

A composite beam bending geometry of interest is illustrated in Figure 2-1. The bottom and top thin film layers are assumed to be two orders of magnitude thinner than the middle layer. We are mostly interested in the top and bottom thin films and will consider the mechanics of the thin films only. If the thin film materials are isotropic elastic media, the constitutive equation between stress and strain can be

written as the following.

$$\begin{aligned}
\epsilon_{xx} &= \frac{1}{E}\left(\sigma_{xx} - \nu\sigma_{yy} - \nu\sigma_{zz}\right) \\
\epsilon_{yy} &= \frac{1}{E}\left(-\nu\sigma_{xx} + \sigma_{yy} - \nu\sigma_{zz}\right) \\
\epsilon_{zz} &= \frac{1}{E}\left(-\nu\sigma_{xx} - \nu\sigma_{yy} + \sigma_{zz}\right)
\end{aligned} \tag{2.1.15}$$

E stands for Young's modulus and ν Poisson's ratio. Notice that deviatoric stress and strain components are all zero in uniform beam bending geometry. For thin film materials, since the strain in z direction due to Poisson contraction is much smaller than the strain in (x,y) direction, we may safely assume that $\epsilon_{zz} = 0$.

$$\begin{aligned}
\epsilon_{zz} &= \frac{1}{E}\left(-\nu\sigma_{xx} - \nu\sigma_{yy} + \sigma_{zz}\right) = 0 \\
\text{Equivalently,} \quad \sigma_{zz} &= \nu(\sigma_{xx} + \sigma_{yy})
\end{aligned} \tag{2.1.16}$$

Given the free boundary condition in y direction, the top and bottom layers are allowed to expand freely in y direction. Since $\sigma_{yy} = 0$ holds,

$$\sigma_{zz} = \nu\sigma_{xx} \tag{2.1.17}$$

Substituting this into the constitutive equation and re-arranging in terms of ϵ_{xx},

$$\begin{aligned}
\epsilon_{xx} &= \frac{1}{E}\left(\sigma_{xx} - \nu^2\sigma_{xx}\right) \\
\epsilon_{yy} &= \frac{1}{E}(-\nu\sigma_{xx} - \nu^2\sigma xx) = \frac{-\nu\epsilon_{xx}}{1-\nu} \\
\epsilon_{zz} &= 0
\end{aligned} \tag{2.1.18}$$

Equivalently, in terms of stress,

$$\begin{aligned}
\sigma_{xx} &= \frac{E}{(1-\nu^2)}\epsilon_{xx} \\
\sigma_{yy} &= 0 \\
\sigma_{zz} &= \frac{\nu E}{(1-\nu^2)}\epsilon_{xx}
\end{aligned} \tag{2.1.19}$$

Note the following expression for the hydrostatic stress.

$$\sigma_{hydro} = \frac{1}{3}\mathrm{Tr}(\boldsymbol{\sigma}) = \frac{E}{3(1-2\nu)}\epsilon_{xx} \tag{2.1.20}$$

The stored elastic strain energy is then given by one half of the scalar product of stress and strain.

$$\begin{aligned} U_{\text{strain}} &= \frac{1}{2}\boldsymbol{\sigma}\boldsymbol{\epsilon} \\ &= \frac{1}{2}\begin{bmatrix} \sigma_{xx} & 0 & 0 \\ 0 & 0 & 0 \\ 0 & 0 & \nu\sigma_{xx} \end{bmatrix} \cdot \begin{bmatrix} \epsilon_{xx} & 0 & 0 \\ 0 & \epsilon_{yy} & 0 \\ 0 & 0 & 0 \end{bmatrix} = \frac{1}{2}\sigma_{xx}\epsilon_{xx} \end{aligned} \tag{2.1.21}$$

Given the geometric factor, the strain in bottom thin film is given by $\epsilon_{xx} = \frac{h}{R}$ and inserting this into the stored strain energy yields the following expression.

$$U_{\text{strain}} = \frac{E}{2(1-\nu^2)}\left(\frac{h}{R}\right)^2 \tag{2.1.22}$$

2.1.3 Thermodynamic potential and electrochemical potential

Expressions of relevant thermodynamic potentials derive from the internal energy expression and Legendre transform. The differential form of a systen's internal energy can be written as the following:

$$dU = TdS + \sum_{i=1}^{M} p_i dq_i + \sum_{j=1}^{N} \mu_j dn_j \tag{2.1.23}$$

Here, p_i and q_i denote the i^{th} pair of conjugate variables that represent the system's intensive and extensive thermodynamic properties. In the differential form, the extensive variables can be viewed as coordinates to the state function U and the intensive variables as the coefficients to the coordinates. Integrating the differential over the extensive variables, S, q_i and n_j, result in the following expression for the total energy

of the system:

$$U = TS + \sum_{i=1}^{M} F_i q_i + \sum_{i=1}^{N} \mu_i dn_i \qquad (2.1.24)$$

The internal energy function U is known as a state function of the system which contains the system's complete thermodynamic information via its partial derivatives. Under experimental conditions, intensive variables such as temperature T are controlled more conveniently than extensive variables and thus, thermodynamic potentials with one or more intensive variables as coordinates are preferred. Legendre transformation fulfills such requirement without any loss of the system's thermodynamic information.

Legendre transformation

A simple example function $f = f(x)$ with one variable can be used to illustrate Legendre transformation. A Legendre transform will introduce a function $g(u)$ where $u = \pm\frac{df}{dx}$. The differential of $f(x)$ may be expressed as the following:

$$\begin{aligned} df = \frac{df}{dx}dx = udx = d(ux) - xdu \\ d(f - ux) = -xdu \\ \frac{d(f - ux)}{du} = -x \end{aligned} \qquad (2.1.25)$$

We define $g(x)$ as the Legendre transformation of $f(x)$, such that

$$g(u) = f(x) - ux = f(x) - x\frac{df}{dx} \qquad (2.1.26)$$

Gibb's free energy

Gibbs free energy, G, represents the thermodynamic potential at typical experimental conditions of constant temperature T and isotropic pressure P.

$$\begin{aligned} G &= U - ST + PV \\ dG &= -SdT + VdP + \sum_{i=1}^{N} \mu_i dn_i \end{aligned} \tag{2.1.27}$$

Chemical potential of an i^{th} species is defined as the partial derivative of Gibbs free energy with respect to the number of i^{th} particles. This quantity denotes that amount of free energy change per each i^{th} particle added to the system.

$$\mu = \left(\frac{\partial G}{\partial N_i}\right)_{T,P,N_{j\neq i}} \tag{2.1.28}$$

Since chemical potential varies with the number of particles, it is often expressed in terms of a constant quantity and quantity dependent on the particle number (or equivalently concentration). The concentration dependence is expressed in terms of activity a_i which is often expressed as the product of concentration (c) and activity coefficient (γ).

$$\mu = \mu_i^o + RTln(a_i) = \mu = \mu_i^o + RTln(\frac{\gamma_i c_i}{\sum_j c_j}) \tag{2.1.29}$$

For ionic species (such as Li^+, electrochemical potential can be defined based on the following rationale.

$$\begin{aligned} \mu_{\mathrm{Li}} &= \mu_{\mathrm{Li}^+} + \mu_{e^-} \\ \text{Since} \quad \mu_{e^-} &= -e\phi \\ \mu_{\mathrm{Li}^+} &= \mu_{\mathrm{Li}} + e\phi = \mu_{\mathrm{Li}}^o + RTln(\gamma_{\mathrm{Li}} \times c_{\mathrm{Li}}) + e\phi \end{aligned} \tag{2.1.30}$$

where ϕ stands for electric potential. Electrochemical potential denotes the amount of energy required to add an ionic species into the solution, often expressed as Joules/mole.

2.1.4 Stress contribution to thermodynamic potential

As mentioned in the above sections, the electrochemical potential for i^{th} component along with stress contribution may be written as the following:

$$\Gamma_i = \mu_i^o + RTln\left(\frac{\gamma_i N_i}{\sum_j N_j}\right) + z_i F\phi_e + V\sigma_{kl}\left(\frac{\partial \epsilon_{kl}}{\partial N_i}\right)_{T,P,N_{m\neq i}} \tag{2.1.31}$$

where σ_{ij} and ϵ_{ij} stand for the stress and strain acting on i^{th} surface in j^{th} direction, z_i the number of moles of electrons a mole of ions contribute, F Faraday's constant, and V the molar volume. For example, we may write down the expression for Li's electrochemical potential under stress in Li_xSi compound.

$$\Gamma_{\mathrm{Li}} = \mu_{\mathrm{Li}}^o + RTln\left(\frac{\gamma_{\mathrm{Li}} x}{1+x}\right) + z_{\mathrm{Li}} F\phi_e + V\sigma_{kl}\left(\frac{\partial \epsilon_{kl}}{\partial N_{\mathrm{Li}}}\right)_{T,P,N_{Si}} \tag{2.1.32}$$

[mention potential solutions of diffusion equation and power law behavior in chapter 2 diffusion part]

2.2 Kinetic processes

Kinetics concerns with the rates of change between systems that are out of equilibrium. The study particularly emphasizes the mechanisms by which the systems change and their kinetic behavior with mathematical descriptions. Here, I will briefly introduce the fundamental formulations of irreversible thermodynamics and descriptions of kinetic processes present in this study: atomic diffusion, ionic diffusion and electrochemical charge transfer process.

2.2.1 Diffusion

According to the classical thermodynamics, intensive quantities will reach identical value if their extensive conjugate variables are allowed to be exchanged. The reversible path to equilibrium, however, is not available for a general non-equilibrium system. The treatment of irreversible thermodynamics, therefore, assumes local equi-

librium, where the thermodynamic description of a small volume (cell) of a system can be described in terms of the local values of thermodynamic potentials. The basic postulate for irreversible thermodynamics states that the local entropy generation in each cell in not negative near equilibrium.

$$\dot{\sigma} \equiv \frac{\partial s}{\partial t} + \nabla \cdot J_s \geq 0 \tag{2.2.1}$$

$\dot{\sigma}$ indicates local entropy generation rate in a cell with volume v_0, given by $\dot{\sigma} \equiv \int_{v_0} \dot{\sigma} dV$. The entropy generation caused by general thermodynamic coordinates derives from the first law of thermodynamics.

$$Tds = du - \sum_i p_i dq_i \tag{2.2.2}$$

Writing in terms of entropy generation and flux, we obtain the following expression for the general local entropy generation.

$$T\dot{\sigma} = -\frac{J_Q}{T} \cdot \nabla T - \sum_i J_i \cdot \nabla p_i \tag{2.2.3}$$

We denote J_i and ∇p_i as the conjugate fluxes and forces. Sometimes, an alternative notation for forces are used. ($F_i = \nabla p_i$) Under the postulate that there is a linear correlation between flux and all possible driving forces, we may write the flux expression in terms of its driving forces.

$$J_1(F_1, F_2, ..., F_N) = \frac{\partial J_1}{\partial F_1} F_1 + \frac{\partial J_2}{\partial F_2} F_2 + ... + \frac{\partial J_N}{\partial F_N} F_N \tag{2.2.4}$$

In short, the notation for flux coefficients run as the following.

$$J_\alpha = \sum_\alpha L_{\alpha\beta} F_\beta \quad \text{where} \quad L_{\alpha\beta} = \frac{\partial J_\alpha}{\partial F_\beta} \tag{2.2.5}$$

For example, an ionic species j^{n+} will experience driving force from chemical potential μ_j and local electric potential ϕ. Since the conjugate extensive variable (dq) for ϕ is

equivalent to the net charge carried by the ionic species $nedc_j$, the driving force can be written as $F_j = -\nabla(\mu_j + ne\phi)$, the electrochemical potential introduced earlier. The electrochemical potential is an example of the diffusion potential which indicates the total conjugate force for a diffusing species. It is also noted here that Onsager's symmetry principle states that the coupling coefficients are symmetric.

$$L_{\alpha\beta} = L_{\beta\alpha} \tag{2.2.6}$$

Diffusion is a broad term indicating the exchange of thermodynamic extensive variables between unit volumes under a driving force. We will now examine detailed flux expressions for two relevant cases, atomic diffusion and ionic diffusion.

Atomic diffusion

Atoms in solids are known to diffuse with and without the chemical effects. In the absence of chemical effects, thermal motions drive atomic diffusion termed self diffusion. Based on experiments with isotopes, this diffusion has been shown to follow Fick's law which relate flux to concentration gradient.[38]

$$J_1 = -D\nabla c_1 \tag{2.2.7}$$

D indicates the mass diffusivity or diffusion coefficient. This is consistent with the general theory stating that flux is proportional to chemical potential gradient, assuming ideal mixture (Raultian behavior) and equilibrium vacancy concentration ($\mu_v = 0$).

In chemically inhomogeneous solids with multiple components and equilibrium vacancy concentration, we may write the flux expression for components as the fol-

lowing,

$$\begin{aligned} J_1 &= L_{11}F_1 + L_{12}F_2 \\ &= -L_{11}\nabla\mu_1 - L_{12}\nabla\mu_2 \\ &= -\left(L_{11} - \frac{c_1}{c_2}L_{12}\right)\nabla\mu_1 \end{aligned} \tag{2.2.8}$$

assuming local equilibrium and thus Gibbs-Duhem relation ($c_1\nabla\mu_1 + c_2\nabla\mu_2 + c_v\nabla\mu_v = 0$). The local variation in volume due to different sized diffusing species is assumed small. Inserting the concentration dependence on chemical potential ($\mu_1 = \mu_1^0 + kT\ln(\gamma_1 c_1)$) yields the expression for intrinsic diffusivity.

$$J_1 = -kT\left(\frac{L_{11}}{c_1} - \frac{L_{12}}{c_2}\right)\left(1 + \frac{\partial\gamma_1}{\partial c_1}\right)\nabla c_1 = D_1\nabla c_1 \tag{2.2.9}$$

The consideration up to this point was done assuming that lattice planes remain unchanged by the diffusion process. However, since local variation in volume arises from diffusion of different-sized species (the effect termed Kirkendall effect) we may devise a volume-fixed frame which conveniently links to the laboratory frame. Assuming that the volume of diffusing species are constant within the entire body, we choose the frame such that there is no flux of volume in any lattice plane as the volume fixed plane. The velocity of this frame with respect to the crystal lattice frame is given by the following

$$v_C^V = (D_1 - D_2)\Omega_1\nabla c_1 \tag{2.2.10}$$

where Ω_1 indicates the volume of diffusing species 1. Assuming that the volume of species 1 and 2 are the same, the flux of species 1 is then given by the following expression.

$$J_1^V = -(X1D_2 + X2D_1)\nabla c_1 = -\widetilde{D}\nabla c_1 \tag{2.2.11}$$

$\widetilde{D}$ is termed interdiffusivity. We observe that Fick's law behavior is expected in both

lab frame and crystal frame.

Ionic diffusion

In an ionic compound or an electrolyte medium, electrochemical potential serves as the diffusion potential.

$$J_1 = -L_{11}\nabla(\mu_1 + ne\phi) \tag{2.2.12}$$

Assuming constant activity coefficient (γ) in dilute solution limit in chemical potential expression ($\mu_1 = \mu_1^0 + kT\ln(\gamma_1 c_1)$), we can expand as the following:

$$\begin{aligned} & J_1 = v_1 c_1 = -M_1 kT\nabla c_1 - M_1 c_1 ne\nabla c_1 \\ \text{with} \quad & D_1 = -M_1 kT, \\ & J_1 = -D_1\nabla c_1 - \frac{D_1 c_1 ne}{kT}\nabla\phi \end{aligned} \tag{2.2.13}$$

where M_1 indicates mobility, the linear coefficient between the driving force and species velocity. The relation between diffusivity and mobility ($D_1 = M_1 kT$) is referred to as Nernst-Einstein equation. This expression for flux holds for ion migration in dilute solution and interstitial diffusion in ionic crystals.

2.2.2 Charge transfer reaction

In the presence of an electric potential difference between two different media, charge transfer reaction takes place. Charge transfer reaction occurring on the electrode surface is often modeled using Butler Volmer kinetics. Butler-volmer equation is a phenomenological equation describing the electrochemical reaction kinetics according to the electrode overpotential. Its derivation follows from the description of the interfacial equilibrium at the electrode surface.

$$Red \leftrightarrow Ox + ne^- \tag{2.2.14}$$

Here, Red and Ox represent the reduced species and oxidized species in general. The number of electrons involves in the overall reaction is denoted as n. The reaction rate for anodic and cathodic reaction follows that of Arrhenius behavior. The overall reaction rate is then represented as the difference between anodic reaction rate and cathodic reaction rate.

$$R = R_a - R_c = k_a C_{red} \times exp^{\frac{(1-\alpha)ne\Delta\phi}{kT}} - k_c C_{ox} \times exp^{\frac{(\alpha)ne\Delta\phi}{kT}} \tag{2.2.15}$$

k_a and k_c represent the anodic and cathodic rate coefficients, respectively. C_{red} and C_{ox} denote the concentration of reduced and oxidized species. $\Delta\phi$ represents the potential difference between electrode potential ϕ_e and solution potential ϕ. α represents the charge transfer coefficient, which in simple terms, represents the ratio of anodic reaction activation energy to the cathodic reaction activation energy. In other words, it represents whether the transition state is closer in energy to anodic product or cathodic product. In this sense, it is also called the symmetric factor and is often assumed to be 0.5 for most cases. If the electrode surface strongly favors reaction in one direction, its value may take the limits of either zero or one.

When in equilibrium, the net reaction rate R is zero; the cathodic reaction rate and anodic reaction rate are the same.

$$\begin{aligned} R_a = R_c = k_a C_{red} \times exp^{\frac{(1-\alpha)ne\Delta\phi}{kT}} &= k_c C_{ox} \times exp^{\frac{(\alpha)ne\Delta\phi}{kT}} \\ k_a C_{red} \times exp\frac{ne\Delta\phi}{kT} &= k_c C_{ox} \end{aligned} \tag{2.2.16}$$

Rearranging the terms,

$$\Delta\phi_{equilibrium} = \frac{kT}{ne} ln\left(\frac{k_c C_{ox}}{k_a C_{red}}\right)$$

This derivation defines the equilbrium electrode potential in terms of kinetic reaction rates and results in identical expression as the Nernst equation. It is also noted that the equilibrium potential is independent of the charge transfer coefficient.

The overpotential is then expressed as the excess potential above the equilibrium

potential, driving the reaction towards a specific direction and electric current.

$$\eta = \Delta\phi - \Delta\phi_{eq} \tag{2.2.17}$$

In the presence of an overpotential, the net reaction rate can be expressed as the following.

$$\begin{aligned} R &= k_a C_{red} \times exp^{\frac{(1-\alpha)ne(\eta+\Delta\phi_{eq}}{kT}} - k_c C_{ox} \times exp^{\frac{-\alpha ne(\eta+\Delta\phi_{eq}}{kT}} \\ &= k_a C_{red} \left(\frac{k_c C_{ox}}{k_a C_{red}}\right)^{1-\alpha} \times exp^{\frac{(1-\alpha)ne\eta}{kT}} - k_c C_{ox} \left(\frac{k_c C_{ox}}{k_a C_{red}}\right)^{-\alpha} \times exp^{\frac{-\alpha ne\eta}{kT}} \\ &= (k_c C_{ox})^{1-\alpha} (k_a C_{red})^{\alpha} \left[exp^{\frac{(1-\alpha)ne\eta}{kT}} - exp^{\frac{-\alpha ne\eta}{kT}}\right] \end{aligned} \tag{2.2.18}$$

The current generated from the reaction rate R and surface area A is $I = AneR$. Re-writing the expression in terms of electric current, we obtain the Butler-Volmer equation

$$I = I_0 \left[exp^{\frac{(1-\alpha)ne\eta}{kT}} - exp^{\frac{-\alpha ne\eta}{kT}}\right] \tag{2.2.19}$$

where $I_0 = Ane(k_c C_{ox})^{1-\alpha}(k_a C_{red})^{\alpha}$.

We may explore the limiting cases for the equation where the overpotential is small ($\eta << kT$) and large ($\eta >> kT$). For small overpotential, we may expand the equation in Taylor series and linearize the behavior. Specifically,

$$\begin{aligned} I &= I_0 \left[exp^{\frac{(1-\alpha)ne\eta}{kT}} - exp^{\frac{-\alpha ne\eta}{kT}}\right] \\ &\approx I_0 \left[1 + (1-\alpha)\frac{ne\eta}{kT} + \left(\frac{(1-\alpha)ne\eta}{kT}\right)^2 ... - 1 + \frac{\alpha ne\eta}{kT} - \left(\frac{\alpha ne\eta}{kT}\right)^2\right] \\ &\approx I_0 \frac{ne\eta}{kT} \end{aligned} \tag{2.2.20}$$

In this region, the current is linearly proportional to the applied overpotential, and thus, follows Ohmic behavior with a constant resistance of $R = \frac{kT}{neI_0}$.

For large overpotential, depending on the sign of the overpotential, either the

cathodic or anodic term will dominate the current expression. Specifically,

$$\begin{aligned} I &= I_0 \left[exp^{\frac{(1-\alpha)ne\eta}{kT}} \right] \text{ for } \quad \eta >> kT \\ I &= -I_0 \left[exp^{\frac{-\alpha ne\eta}{kT}} \right] \text{ for } \quad \eta << -kT \end{aligned} \tag{2.2.21}$$

This region is called Tafel response and is characterized by semi-log behavior (ln(I) $\propto \eta$).

2.2.3 Dissipation rate

Kinetic processes often involve various energy dissipation modes and this can be understood in terms of entropy production rate. The local entropy production rate can be understood in terms of the volume normalized extensive quantities (equivalently, density of extensive quantities).

$$\begin{aligned} \frac{\partial s}{\partial t} &= \frac{1}{T}\frac{\partial u}{\partial t} - \frac{1}{T}\Sigma_j \psi_j \frac{\partial \xi}{\partial t} \\ &= -\frac{1}{T}\nabla \cdot \vec{J_u} + \frac{1}{T}\vec{\Sigma_j}\psi_j \nabla \cdot \vec{J_j} \end{aligned} \tag{2.2.22}$$

The time derivative of extensive quantity densities are re-written in terms of flux using divergence theorem in equation (2.2.22). Since $\vec{A}\nabla \cdot \vec{B} = -\vec{B} \cdot \nabla \vec{A} + \nabla \cdot (\vec{A}\vec{B})$, we may further re-write as the following.

$$\frac{\partial s}{\partial t} = (\vec{J_u} \cdot \nabla \frac{1}{T} - \Sigma_j \vec{J_j} \cdot \nabla \left(\frac{\psi_j}{T} \right) - \nabla \cdot \left(\frac{\vec{J_u} - \Sigma_j \psi_j J_j}{T} \right) \tag{2.2.23}$$

For non-conserved quantities such as entropy, we may write the following expression in terms of entropy flux and entropy production rate.

$$\frac{\partial s}{\partial t} = -\nabla \cdot \vec{J_s} + \dot{\sigma_s} \tag{2.2.24}$$

Comparing equations (2.2.22) and (2.2.23), we obtain the following expression for entropy flux and entropy production rate.

$$\begin{aligned} \dot{\sigma_s} &= J_u \cdot \nabla \frac{1}{T} - \Sigma_j \vec{J_j} \cdot \nabla \left(\frac{\psi_j}{T} \right) \\ \vec{J_s} &= \frac{\vec{J_u}}{T} - \frac{1}{T} \Sigma_j \psi_j \vec{J_j} \end{aligned} \tag{2.2.25}$$

Here, we note that

$$du = \frac{dQ}{V_0} + \Sigma_j \psi_j d\xi_j \tag{2.2.26}$$

Assuming the local equilibrium ($TdS = \frac{dQ}{V_0}$),

$$\vec{J_u} = \vec{J_Q} + \Sigma_j \psi_j \vec{J_j} \tag{2.2.27}$$

Comparing these to the previous expression of entropy production rate,

$$\dot{\sigma} = \vec{J_Q} \cdot \nabla \frac{1}{T} + \Sigma_j \psi_j \vec{J_j} \cdot \nabla \frac{1}{T} - \Sigma_j \vec{J_j} \cdot \nabla \left(\frac{\psi_j}{T} \right) \tag{2.2.28}$$

Since $\nabla \left(T \times \frac{1}{T} \right) = \frac{1}{T} \nabla T + T \nabla \frac{1}{T}$, we may expand and re-write the expression as the following.

$$\begin{aligned} \dot{\sigma} &= \vec{J_Q} \cdot \nabla \frac{1}{T} + \Sigma_j \vec{J_j} \left(\psi_j \cdot \nabla \frac{1}{T} \right) - \Sigma_j \frac{\vec{J_j}}{T} \cdot \nabla \psi_j - \Sigma_j \vec{J_j} \left(\psi_j \cdot \nabla \frac{1}{T} \right) \\ &= \vec{J_Q} \cdot \nabla \frac{1}{T} - \Sigma_j \frac{\vec{J_j}}{T} \cdot \nabla \psi_j \end{aligned} \tag{2.2.29}$$

We then obtain the final expression of the energy dissipation rate as the following.

$$T\dot{\sigma} = -\frac{J_Q}{T} \cdot \nabla T - \Sigma_j \vec{J_j} \cdot \nabla \psi_j \tag{2.2.30}$$

It is noted here that the energy dissipataion rate of a kinetic process depends on the product of flux and the gradient of the conjuate intensitve quantity.

2.3 Experimental methods

In this section, I will briefly introduce the experimental techniques used in the study and some of the technical features of the device design. The subsections include two electrochemical techniques used in the study and electrode deposition techniques on flexible substrates.

2.3.1 Electrochemical impedance spectroscopy

The reactions that occur at the electrochemical interface in general are by nature diverse and non-linear. Some of the key reactions include polarization of the surface, the double layer capacitance charging, diffusion of reactants and products in the electrolyte and the charge transfer reaction. While Butler Volmer model captures the non-linearity based on phenomenological descriptions, an experimental technique involving the characterization and parametrization of the surface reactions is desired. Electrochemical impedance spectroscopy serves as a crucial tool for this purpose. The tool utilizes the fact that the physical processes mentioned above have different timescale, and thus react differently to the high and low frequency potential perturbations. By providing a perturbative sinusoidal electric potential to the electrode and measuring the electric current response, the technique measures the total impedance and phase difference at each frequency. By analyzing this data with respect to the equivalent circuit, we achieve characterization of the surface reactions.

A typical equivalent circuit for the electrochemical surface with reactions mentioned above can be constructed as Figure 2-2. Warburg impedance indicates the impedance for diffusion of reactants and products. For such construction, the overall impedance can be expressed as a function of frequency.[39]

$$\begin{aligned} Z(w) = R_s + \frac{R_p + \sigma\omega^{-0.5}}{\sigma\omega^{0.5}(C_d+1)^2 + \omega^2 {C_d}^2 (R_p + \sigma\omega^{-0.5})^2} \\ + i\frac{[\omega C_d (R_p + \sigma\omega^{-0.5})^2 + \sigma\omega^{-0.5}(C_d\sigma\omega^{-0.5}+1)]}{(C_d\sigma\omega^{0.5}+1)^2 + \omega^2 {C_d}^2 (R_p + \sigma\omega^{-0.5})^2} \end{aligned} \tag{2.3.1}$$

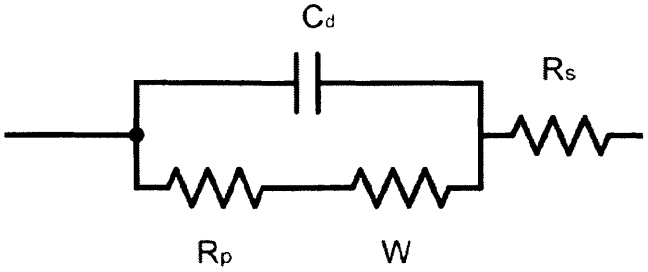

Figure 2-2: Equivalent circuit for an electrochemical interface with polarization resistance (R_p), Warburg impedance (W), double layer capacitance (C_d), and solution resistance (R_s)

Here, R_s, R_p, C_d refer to solution resistance, polarization resistance and double layer capacitance, respectively. w refer to angular frequency ($w = 2\pi f$ where f is frequency). σ refers to the electrode surface characteristic

$$\sigma = \frac{RT}{\sqrt{2}n^2F^2A}\left(\frac{1}{D_o^{1/2}C_o(x,t)} + \frac{1}{D_r^{1/2}C_r(x,t)}\right) \tag{2.3.2}$$

where A refers to electrode surface area, x distance from electrode surface, t time, RT the gas constant multiplied by temperature, n number of electrons involved in the reaction, F Faraday's constant, D_o and D_r the diffusivity constant for oxidant and reductant, c_o and c_r the concentration for oxidant and reductant. The Walberg impedance can be expressed in terms of σ as the following.

$$W = \left(\frac{2}{\omega}\right)^{\frac{1}{2}}\sigma \tag{2.3.3}$$

In the high frequency regime, simplification to the following expression is possible.

$$Z(\omega) = \left(R_s + \frac{R_p}{1+\omega^2R_p^2C_d^2}\right) - i\left(\frac{\omega R_p^2C_d}{1+\omega^2R_p^2C_d^2}\right) \tag{2.3.4}$$

Similarly in the low frequency regime, the expression gets reduced to the following.

$$Z(\omega) = \left(R_s + R_p + \frac{\sigma}{\sqrt{\omega}}\right) - i\left(\frac{\sigma}{\sqrt{\omega}} + 2\sigma^2 C_d\right) \tag{2.3.5}$$

In either cases, it is convenient to plot the impedance in terms of its real component and imaginary component. Such plot construction is called Nyquist plot and is often used to visualize the data from electrochemical impedance spectroscopy.

2.3.2 Chronopotentiometry

An electrochemical reaction is unique in the ability to control the reaction rate via controlling the electric current within the system. Since an electrochemical reaction always involves the exchange of electrons, artificially setting the amount of electric current sets the overall kinetics of the electrochemical system. With the emergence of advanced electronics, it is possible to feed a precise amount of electric current to the electrochemical system.

Chronopotentiometry is the experimental method in which a defined amount of electric current is flowed into the system for a defined amount of time. At the same time, the potential difference between the working (the electrode of interest) and counter electrode is measured, to probe the energetic information of the electrochemical reaction in progress. The technique involving controlled current is also termed galvanostatic as opposed to potentiostatic techniques which indicate the techniques involving controlled potential difference.

In this thesis, chronopotentiometry is used in the context of preparing specific composition of Li_xSi alloy. As deposited silicon thin film may be alloyed with lithium via setting up an electrochemical cell. The cell used in this work consists of silicon thin film and lithium metal electrodes, sandwiching a layer of standard battery grade Lithium electrolyte. Since there exists a difference in lithium chemical potential difference between the two electrodes, simply connecting the circuit results in alloying reaction between silicon and lithium. Specifically, lithium from lithium metal side will migrate into silicon electrode in the form of lithium ions and electrons. Nevertheless,

if the two electrodes are directly connected, the reaction occurs at a rate that is not precisely known or controlled. Since reaction rate often affects the morphologies of final product, controlling the reaction rate helps preparing an alloy with specific morphologies and microstructure. The typical nomenclature for reaction rate in battery reactions involves 'C rate' where 1C rate indicates the rate where full discharge of the cell occurs in an hour. Similarly, 2C and C/2 rates indicate full discharge in 1/2 hour and 2 hours respectively. The preparation of specific composition is possible via controlling the amount of time; stopping the reaction after 1/2 hour at 1C rate would give half-discharged reaction product. In addition, certain extent of information about the reaction product can be obtained from the measured potential when electric current is flowing.

2.3.3 Thin film deposition

With the development of electronics industry, various thin film deposition techniques with accuracy of up to 1nm have been developed. In large, the techniques can be divided into physical vapor deposition and chemical vapor deposition. Physical vapor deposition involves melting or evaporation of target material via external stimuli such as heating, plasma or pulsed laser. Chemical vapor deposition involves dissociation of precursor gas via external stimuli such as plasma or heat and deposition of the dissociated product. While the method has been successful in its versatility - control of crystallinity, thickness, layer-by-layer deposition or film stress, the method is capable of depositing only those with gaseous precursors available.

Most thin film depositions in this study are done via physical vapor deposition, especially the electron-beam assisted evaporator. Most materials with melting temperature lower than 2000 degree Celsium can be deposited with relatively easy steps. The method heats up target material above melting temperature, reaching a sufficient level of vapor pressure for deposition. The rate of deposition is determined from its vapor pressure in the vacuum chamber and is measured by quartz crystal microbalance. The deposition is performed at a constant rate, since the growth product may have different film characteristics such as defect density, grain size or crystallinity at

different deposition rates.

2.3.4 Electrode design on flexible substrates

With the rising interest on flexible electronics and wearable devices, electrode patterning on various flexible substrates have been attempted.[40–44] Some criteria for the choice of flexible substrates include mechanical properties, size availability or chemical stability. A few popular choices include polyethylene terephthalate (PET), polyimide (PI) and polydimethylsiloxane (PDMS).

Since small scale currents are being harvested in the works of this thesis, highly conductive metal electrodes such as noble metals are desired. Nevertheless, the adhesion of these metals on flexible substrates have been reported to be poor. Adhesion layers such as chromium or titanium have been reported to improve electrode stability.[45] In addition, the compatibility issue arises between metal thin films and polymer substrates. For instance, while extensive studies have recently been performed on generating a stable metal electrode on PDMS substrate, it has been difficult to achieve stable electrodes with stretchability on PDMS. When deposited via physical vapor deposition, metal thin films with relevant adhesion layers often results in unstable adhesion and micro-crack formation, as illustrated in Figure 2-3. Solutions utilizing wavy morphology[46] or interconnected patches[47] have been proposed, however, the non-conventional geometry has been limiting in several applications.

On the other hand, adhesion on substrates such as PET or PI have been reported to be sufficiently strong.[48] Especially, silver thin films with chromium adhesion layer on PI substrates have been reported to survive sticky tape tests. Relatively weak adhesion of Ag thin films on PET substrates is reported to be improved by the use of polymer primer.

Another important feature in designing electrodes on flexible substrates was thin film stress. Unlike brittle silicon wafers, flexible substrates such as kapton tape (PI) were easily bent when deposited with metal electrode film. For instance, when deposited with 100nm of chromium or platinum, the kapton tapes rolled spontaneously and significantly that further processing on the electrodes was very difficult. Tests

Figure 2-3: Morphology of 100nm gold thin film deposited with thin Ti adhesion layer on PDMS. Although the film remains conductive, we observe numerous cracks in the film and island type growth

reveal that using silver with thickness greater than 40nm acts as effective current collector without much film stress. For the works in this thesis, 100nm silver electrode or 50nm/50nm silver/platinum electrodes on PI were used as current collectors.

Chapter 3

Electrochemically driven Mechanical Energy Harvesting[1]

In this chapter, I report a new type of mechanical energy harvester operative in the low-frequency regime. The device uses the stress-composition coupling in electrochemically active materials, such as partially Li-alloyed Si or Ge.[49][50] The coupling between mechanical stress and lithiation thermodynamics and kinetics[51] has been widely recognized in high-capacity anodes of lithium ion (Li^+) batteries, but was usually regarded as an adverse effect.[49][21][52] Here we demonstrate that mechanical bending induces different stress states in two identical partially Li-alloyed Si electrodes, which drives Li^+ migration and generates electricity. The prototype generator demonstrates power density of $0.48 mW/cm^2$ at 0.3Hz. Our thermodynamic and mechanics analyses lay a theoretical foundation for the device design and optimization.

[1]Parts of this work was reproduced with permission from Kim, S. *et al.* Electrochemically driven Mechanical Energy Harvesting. *Nat. Commun.* 7 10146, under the Nature Publishing Group author license policy and Creative commons licenses

3.1 Thermodynamic working principle and device design

In an electrochemical cell that utilize Li^+ ion migration, the voltage (E) between two electrodes is linked to the difference in lithium chemical potential between anode and cathode. Specifically, for a reaction coordinate x,

$$E(x) = -\frac{\mu_{\text{Li}}^{\text{cathode}}(x) - \mu_{\text{Li}}^{\text{anode}}(x)}{F} \tag{3.1.1}$$

Reaction coordinate x may refer to the composition of cathode or anode depending on the cell configuration. For instance, x in Li_xCoO_2 against Li metal anode may be the case. F stands for Faraday's constant. This voltage difference refers to the open circuit voltage, or equivalently the equilibrium voltage between the two electrodes.

Based on the derivation from section 2.1.3, an expression for chemical potential of lithium with different stress contributions in Li_xSi can be derived as the following:

$$\mu_{\text{Li}} = \mu_{\text{Li}}^{o} + RTln\left(\frac{\gamma_{\text{Li}}x}{1+x}\right) + V\sigma_{kl}\left(\frac{\partial\epsilon_{kl}}{\partial N_{\text{Li}}}\right)_{T,P,N_{\text{Si}}} \tag{3.1.2}$$

In the case of thin Li_xSi film bending, we showed in section 2.1.2 that the deviatoric stress and strain components are zero. Thus, the hydrostatic components can be expressed with Einstein summation.

$$V\sigma_{kl}\left(\frac{\partial\epsilon_{kl}}{\partial N_{\text{Li}}}\right)_{T,P,N_{m\neq\text{Li}}} = V\sigma_{ii}\left(\frac{\partial\epsilon_{ii}}{\partial N_{\text{Li}}}\right)_{T,P,N_{m\neq\text{Li}}} \tag{3.1.3}$$

In the linear elasticity and small strain limit, change in volume can be expressed in terms of hydrostatic strain components.

$$\frac{V}{V_0} = (1+\epsilon_{11})(1+\epsilon_{22})(1+\epsilon_{33}) \approx 1 + \epsilon_{11} + \epsilon_{22} + \epsilon_{33} \tag{3.1.4}$$

Based on this, the stress contribution to chemical potential may be simplified to the

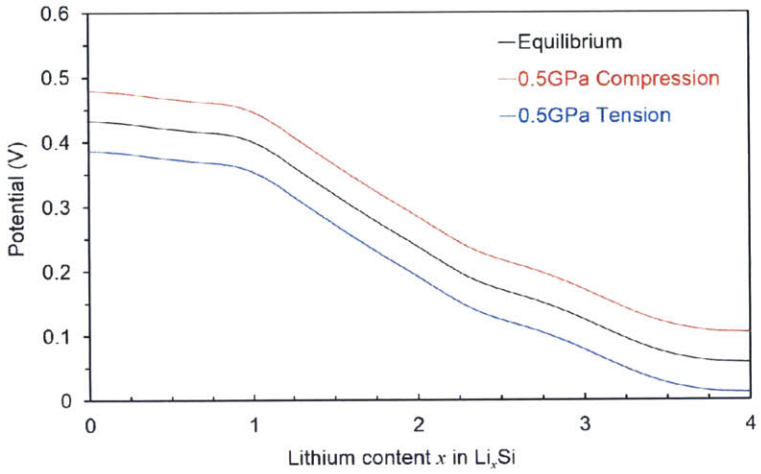

Figure 3-1: Equilibrium voltage difference between Li_xSi and Li according to composition without contribution from stress (black), with 0.5GPa tension (blue) and with 0.5GPa compression. (red)

following.

$$V\sigma_{ii}\left(\frac{\partial \epsilon_{ii}}{\partial N_{\mathrm{Li}}}\right)_{T,P,N_{\mathrm{Si}}} = V\sigma_{ii}\left[\left(\frac{\partial \epsilon_{ii}}{\partial V}\right)\left(\frac{\partial V}{\partial N_{\mathrm{Li}}}\right)\right]_{T,P,N_{\mathrm{Si}}} \approx \sigma_{ii}\overline{V_{\mathrm{Li}}} \tag{3.1.5}$$

where $\overline{V_{\mathrm{Li}}}$ indicates the partial molar volume of lithium inside Li_xSi. It is assumed that this quantity is constant over a wide range of composition change, as is observed experimentally.[53] The difference in chemical potential between Li_xSi and Li metal at different compositions have been computed via first principles calculations by Chevrier and Dahn.[54] Figure 3.1 illustrates this potential difference in terms voltage with and without contributions from different amount of hydrostatic stress.

Based on this, we may develop an energy harvester by introducing different stress states in two electrodes otherwise identical. Figure 3-2 illustrates the working principle of the energy harvester, consisting of two partially Li-alloyed electrodes sandwiching a layer of electrolyte. In the initial stress-free condition, the two electrodes are isopotential (point A in Fig. 3-2a and I in Fig. 3-2b). Bending the device generates net tension in one electrode and compression in the other (points B and C in Fig. 3-2a and II in Fig. 3-2b). The asymmetric stress creates a chemical potential difference that drives Li^+ ion migration from the compressed to the tensed electrode through

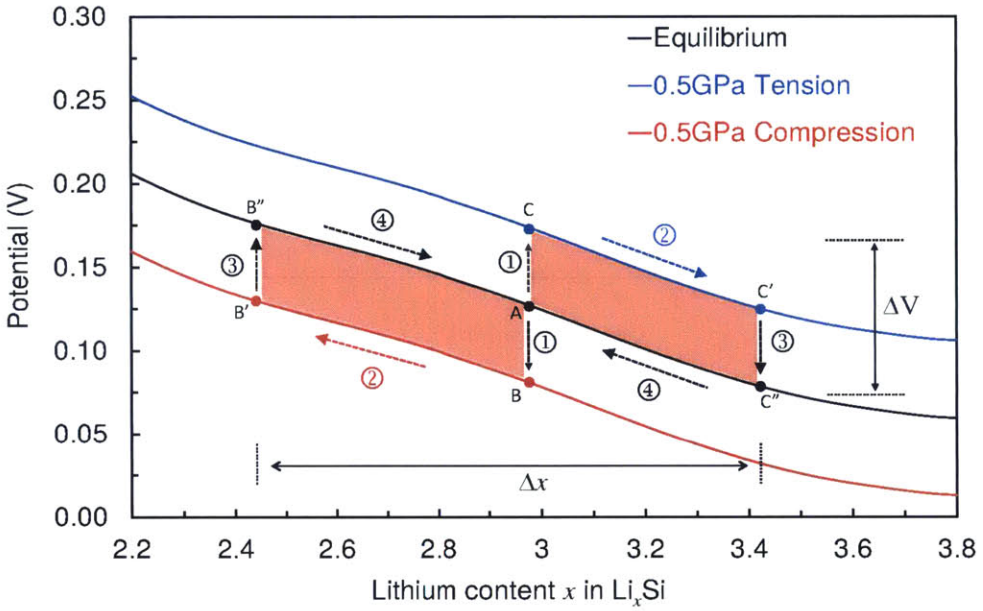

Figure 3-2a: The working principle behind the mechanical energy harvesting device. ① Upon introducing different stress states by bending, a chemical potential difference develops between two electrodes. ② When the electrodes are connected by an external circuit, new equilibrium under the stress states are established by Li^+ migration. ③ and ④ Once the stresses are removed, the lithiation states return back to the original equilibrium state. The area covered by this cycle in red measures the energy output obtained.

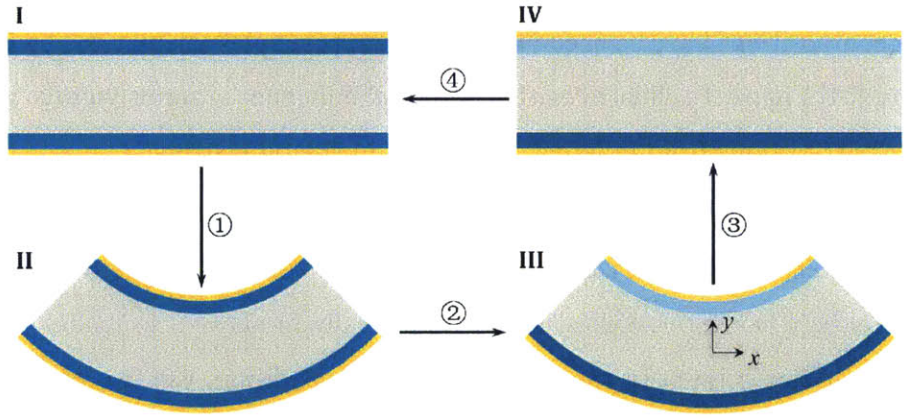

Figure 3-2b: Schematics of the cross section of the device in operation.

the electrolyte. At the same time, to maintain charge neutrality, electrons flow in the outer circuit, also from the compressive to the tensile sides, generating electrical power. The Li^+ migration continues until the potential difference vanishes (points B' and C' in Fig. 3-2a and III in Fig. 3-2b), establishing new equilibrium states on the two electrodes with different Li concentration. When the external stresses are removed by unbending the device, the chemical potential shifts on the electrodes (from point B' to point B" and from point C' to point C" in Fig. 3-2a and III-IV in Fig. 3-2b). The difference in lithium concentration between the electrodes drives Li^+ ion migration in the opposite direction (from point B" and C" to A in Fig. 3-2a and IV-I in Fig. 3-2b), thus discharging the device. The device goes back to its original equilibrium state and may go through this cycle multiple times provided that it operates in the viscoelastic regime without any irreversible damage. The electrical energy generated is equivalent to the potential difference multiplied by the amount of Li^+ migrated, as illustrated as red-colored area in Fig. 3-2a.

3.2 Device Fabrication

Guided by this vision, we developed a prototype generator, consisting of two identical electrodes sandwiching a separator soaked with electrolyte. I will briefly outline the experimental procedures and details that were considered explicitly during the device fabrication.

We used amorphous Li_xSi ($x \approx 3.1$) thin film as the electrodes for its mechanical flexibility and reasonable lithiation and delithiation rates.[55] Ethylene carbonate (EC) mixed with ethyl methyl carbonate (EMC), $LiPF_6$ and micro-porous polypropylene monolayer[56] were used as the electrolyte, lithium salt and separator, respectively. We selected polyimide as the substrate to which the electrodes attach and Ag current collectors for their strong adhesion and stretchability.[48] The polyimide substrates were encapsulated by castable rubber, such as polydimethylsilane (PDMS) or polyurethane. Figure 3-3 shows the schematics and picture of the device. Each Li_xSi electrode is 250nm thick, about two orders of magnitude thinner than the sep-

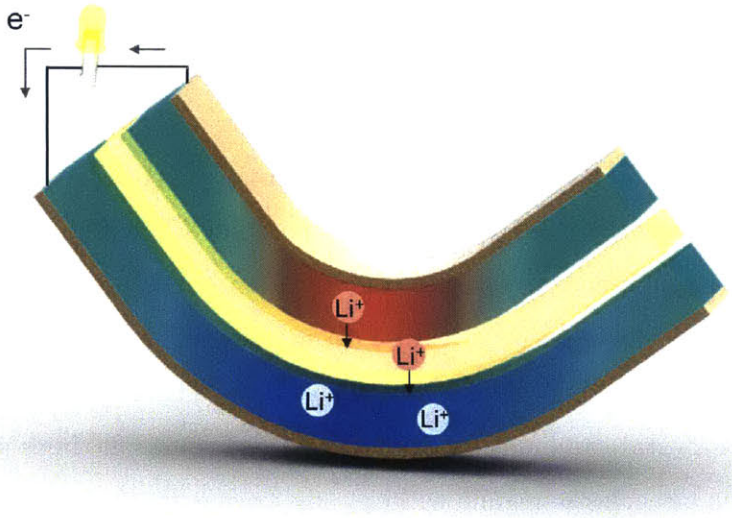

Figure 3-3a: Schematic view of the device design. Compressed region is illustrated in red while the tensed region is illustrated in blue. Lithium ions migrating from the compressed plate to the tensed plate are shown with arrows. The electrolyte soaked separator is drawn in yellow.

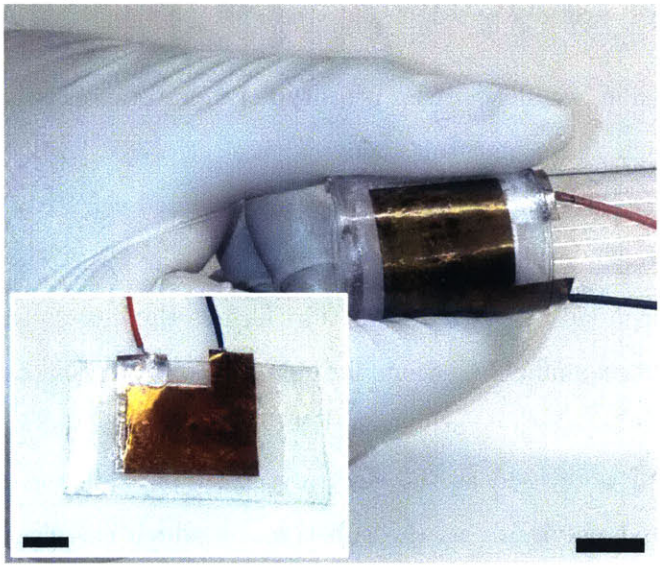

Figure 3-3b: An image of the actual device with a bending unit. Both scale bars indicate 1cm.

arator layer (25μm). The thin-film configuration of the device allows large-curvature bending. Upon bending, the top, compressed electrode becomes an anode, while the bottom, tensed electrode a cathode. The device functions as an energy harvester, and because stress-driven Li^+ ion diffusion conforms to the Onsager linear-response behavior, it is expected to exhibit a decent efficiency even with miniscule loads (that is, no threshold behavior), converting mechanical energy input into electrical energy output.

3.2.1 Flexible substrate choice and electrode deposition

We chose Kapton Polyimide (PI) film as the flexible substrate. PI films provide flexibility, chemical compatibility with lithium ion electrolytes and strong adhesion between the film and electrode materials.[48] The device fabricated on several other flexible substrates resulted in electrode film cracking, little electrical conductivity or delamination during electrochemical lithiation step. On PI substrate, current collector layers consisting of 75nm Ag and 25nm Pt are deposited using electron beam evaporator at $2 Å s^{-1}$ rate. Between the current collector and PI lies a 15nm layer of Cr for better adhesion. Current collectors made only of 100nm Cr or Pt layer resulted in significant bending of Kapton tape either from film stress or heating of PI substrate during deposition. Current collector made entirely of silver had potential alloying of silver with lithium.[57] Thus, the composite layer of silver and platinum was chosen as current collector. On the current collector film, amorphous Si electrode of 75nm (Kurt Lesker, p-type) is deposited using e-beam evaporator. Silicon film thickness (75 nm) was selected carefully to avoid potential structural inhomogeneities such as pores and cracks during extensive cycling tests according to previous studies.[55] A 5nm Ti or Cr adhesion layer was used between the current collector and Si to take account of the lattice constant mismatch. A small region of Ag was left free of silicon for electrical connection.

3.2.2 Electrochemical lithiation

Lithium was inserted into silicon electrochemically via chronopotentiometry. An electrochemical cell consisting of the Si on PI, electrolyte (ethylene carbonate:ethyl methyl carbonate = 1:1 with $LiPF_6$, Novolyte) soaked separator (Celgard 2500) and thick Li foil (Alfa Aesar, 1.5 mm thick) was lithiated using Gamry Reference 3000 potentiostat. Most lithiation was performed at C/2, up to 80% of the theoretical capacity (2,880 $mAhg^{-1}$ out of 3,600 $mAhg^{-1}$). This corresponds to the film composition of approximately $Li_{3.1}Si$. The low cutoff voltage was set to 0.05 V to avoid nucleation of crystalline phase and ensure that the film remains as homogeneous as possible as an amorphous Li-Si alloy.[16] Previous studies have reported that amorphous Si thin films lithiated at C/10 remain smooth to nanometre scale.[23] Control experiments performed with films lithiated at C/2 and C/10 produced identical result within the scope of error.

3.2.3 Device assembly and testing

Device assembly and testing. The electrode prepared above was mounted onto thin polydimethylsiloxane film (PDMS, Sylgard 184, Dow Corning Chemical) for easy handling and encapsulation. PDMS films were prepared by mixing the elastomer with hardener at 10:1 mass ratio and spin-coating onto a 4 inch wafer at 100rpm for 1minute. The film was cured at 100°C for 10 minutes. Paraffin wax was then dissolved onto PDMS as illustrated in previous report to avoid gas and vapor permeability in PDMS.[58] When extra inhibition to gas permeation was required, for example, in repetitive bending test, the entire device was encapsulated in mylar bags often used to manufacture pouch type secondary batteries. The electrode on PI was bonded to cured PDMS by using a thin layer of uncured PDMS as glue. The electrode was then cut in half to comprise the bottom and top electrodes of the energy-harvesting device. The two electrodes were placed on top of each other, separated by a layer of electrolyte-soaked separator (Celgard 2500) and were sealed using uncured PDMS on the sides. To eliminate any possible difference in electrochemical potential or compo-

sition between the top and bottom electrode, the two electrodes were left connected in short-circuit via external wire for at least 2 hours. Bending tests were performed either by finger tapping or by servo motor (HS-7966HB, Hitec). A custom repeatable bending station was constructed using the servo motor, a 32 pitch gear (Servocity), a pinion and Arduino controller. The strain rate was approximately 1% per second if not specified otherwise.

3.3 Mechanics analysis of the device

Mechanics analysis provides insight into the energy conversion efficiency. Fig 3-1b illustrates the bending geometry. Bending the thin-film device generates compressive and tensile strains of equal magnitude $\epsilon_{xx} = \pm h/R$ on the top and bottom electrodes, respectively, where R is the radius of curvature and h the half thickness of the thin-film device. The stress state is obtained under the assumption of elastic deformation. Assuming a plane-stress condition along the y-direction (see Fig. 3-1b for the coordinates), the stress on the bottom electrode can be written as follows,

$$\sigma_{xx} = \frac{E}{(1-\nu^2)}\frac{h}{R}, \quad \sigma_{zz} = \frac{\nu E}{(1-\nu^2)}\frac{h}{R}, \quad \sigma_{yy} = 0 \tag{3.3.1}$$

where E is the Young's modulus and ν the Poisson's ratio. The chemical potential difference between the two electrodes is only related to the difference in the hydrostatic stress $\sigma_{hydro} = \mathrm{Tr}(\boldsymbol{\sigma}/3)$

$$\Delta\mu = \Omega_{\mathrm{Li}}\frac{E}{1-\nu}\frac{2h}{3R} \tag{3.3.2}$$

where $\Omega_{\mathrm{Li}} = 14.95\text{Å}^3$ is the estimated partial molar volume of Li in $\mathrm{Li}_x\mathrm{Si}$.[53][59] This gives a pressure sensitivity of 93mV per GPa, close to a recent experimental measurement of 110mV per GPa.[52]

It is noted that the deviatoric part of the stress tensor $\boldsymbol{\sigma}_{\text{deviatoric}} \equiv \boldsymbol{\sigma} - \sigma_{hydro}\boldsymbol{I}$ does not couple to the chemical potential, where I is the identity tensor. Instead, the deviatoric stress $\sigma_{\text{deviatoric}}$ can induce plastic shear in the material whenever it exceeds

the yield strength, according to the J2 flow rule, but does not generate electrical energy. The total strain-energy (U_{strain}) can be decoupled into the hydrostatic part and the deviatoric part, as:

$$U_{\text{strain}} = \frac{E}{2(1-\nu^2)}\left(\frac{h}{R}\right)^2 = U_{\text{hydro}} + U_{\text{deviatoric}} \tag{3.3.3}$$

with

$$U_{\text{hydro}} = \frac{\sigma_{\text{hydro}}^2}{2B}, \quad B = \frac{E}{3(1-2\nu)} \tag{3.3.4}$$

where B is the bulk modulus. Only the hydrostatic component U_{hydro} can be used for electricity generation, which also varies upon lithium insertion and extraction. Assuming all of U_{hydro} can be utilized for electricity generation, while all of is wasted, an ideal efficiency can be expressed as

$$\eta \equiv \frac{U_{\text{electrical}}}{U_{\text{strain}}} = \frac{U_{\text{hydro}}}{U_{\text{strain}}} = \frac{(1-2\nu)(1+\nu)}{3(1-\nu)} \tag{3.3.5}$$

For ν=0.25,[60] an idealized efficiency of 27.8% is obtained. Interestingly, the energy conversion efficiency is independent of the YoungâĂŹs modulus, and maximizes at ν=0. The total amount of lithium that is expected to transport across the electrolyte in order to completely relax σ_{hydro} is

$$\Delta N_{\text{Li}} = \frac{V_{\text{one-side}}}{\Omega_{\text{Li}}}\frac{Tr(\sigma)}{3B} = \frac{V_{\text{one-side}}}{\Omega_{\text{Li}}}\left(\frac{1-2\nu}{1-\nu}\right)\left(\frac{h}{R}\right) \tag{3.3.6}$$

where $V_{\text{one-side}}$ is the volume of one Li_xSi electrode affected by the radius of curvature and $V_{\text{one-side}}/\Omega_{\text{Li}}$ the amount of Li present in the affected volume determined by previous reports.[22] It is noted that a thicker electrode increases the amount of migrating Lithium and hence the capacity, however, it may also increase the probability for developing structural inhomogeneities such as cracks during lithiation or bending.

3.4 Electrical energy output of the device

Just like photovoltaic energy harvesters, one could characterize a mechanical energy harvester by open-circuit voltage or short-circuit current. I will characterize the harvester and its physics based on its electrical energy output including open circuit potential, short circuit current, efficiency, bending direction dependence and frequency dependence on the output.

3.4.1 Open circuit potential

As mentioned in Chapter 2, open circuit potential measures the difference in equilibrium chemical potential of lithium between two electrodes. In this case, the difference is entirely caused by mechanical stress input and will be equivalent to ΔV illustrated in Figure 3-2a. The open-circuit voltage measured by bending the device in the same direction for 30seconds and resting the device for another 30 seconds with bending force released is shown in Figure 3-4a.

The applied radius of curvature was approximately 1cm, corresponding to a maximum tensile stress of 0.018GPa generated in the electrodes. Since the yield stress of amorphous Li_xSi is 1GPa, the material deforms within its elastic regime.[61] We note that there exists a background potential (nonzero rest potential), which might be due to any unintentional inhomogeneity in composition between the two electrodes or side reactions such as a solid electrolyte interface (SEI) layer formation. The open-circuit voltage increases upon bending and recovers its resting potential once the bending force is released. This trend is consistent with the relationship between the chemical potential difference and the applied radius of curvature ($\Delta\mu \sim R^{-1}$), shown in Equation 3.3.2. This inverse relation between measured open circuit voltage and radii of curvature is well illustrated in Figure 3-5. We used experimentally measured value of Young's modulus (25GPa) for lithiated amorphous silicon thin film, interpolated with rule of mixture for the specific composition we used.[61] Figure 3-5 also shows the predicted hydrostatic stress, voltage, and measured voltage values at six different radii of curvature. The measured open-circuit voltages agree well with the predicted

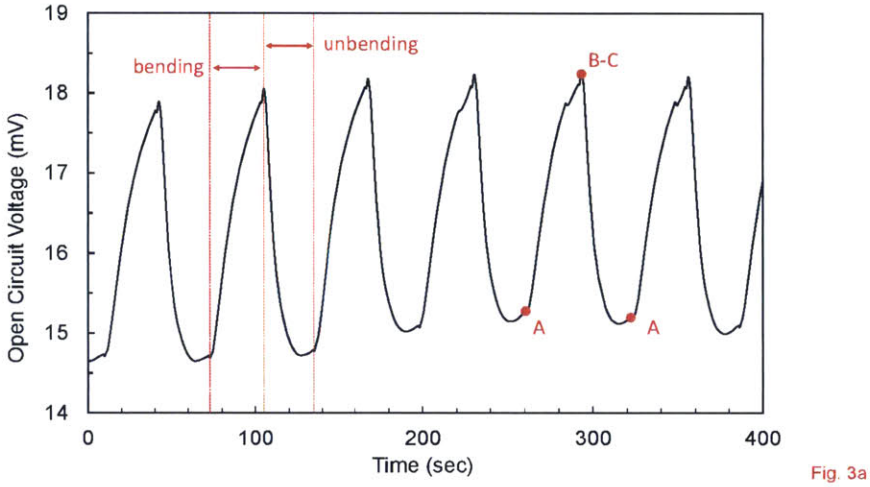

Figure 3-4a: The open circuit voltage measured from simple bending of the device. The measured values show clear voltage peaks during bending and releasing the device, each with 30 s interval. Each alphabetical point corresponds to the bending geometry illustrated in Figure 3-2a.

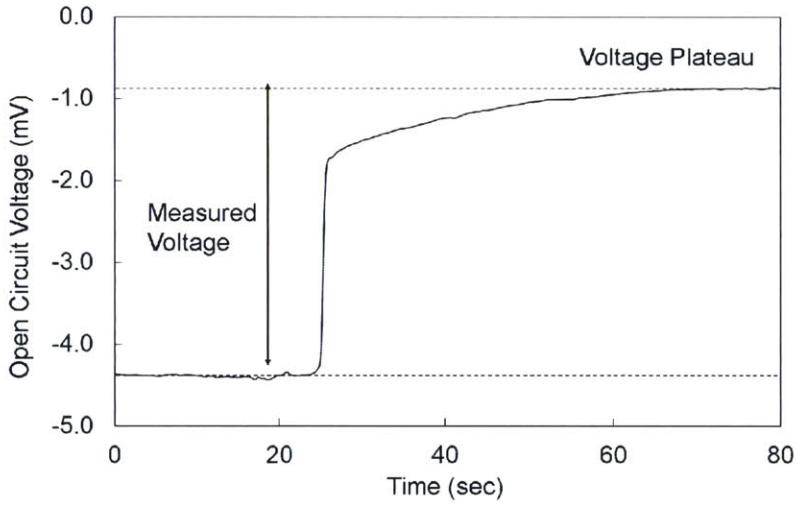

Figure 3-4b: The open circuit voltage reaching a plateau after sufficient bending duration.

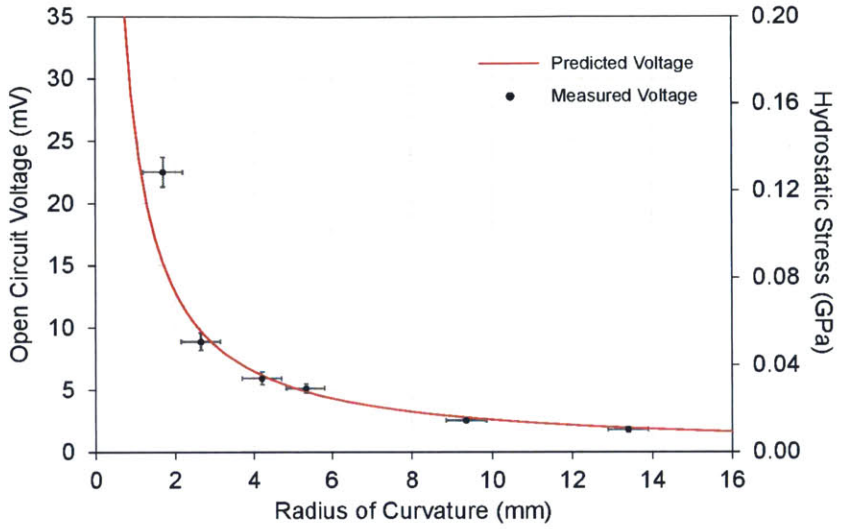

Figure 3-5: The predicted open-circuit voltage and hydrostatic stress according to the radii of curvature, operated in the elastic regime. Standard error resulted from at least five measurements for each radius of curvature is included. The measured voltage values agree well with the predicted values.

values.

Open circuit voltage during alternative bending direction is also measured. Bending is defined in two different directions, 'forward' direction and 'backward' direction. While bending in the forward direction, positive voltage peak is obtained. The peak voltage reaches up to 23mV at the radius of curvature of 0.17cm, in good agreement with the predicted value. Followed by the voltage decay, we observe a voltage peak in the opposite direction during backward bending. The bending experiment generates voltage peaks in a repeatable manner. The general increase in the background voltage may indicate that one electrode is accumulating more damage than the other as the unit is being bent in alternating direction in a severe manner. For instance, the initially compressed electrode may result in more plastic flow compared to the other during the experiment, since the initial damage was more significant.

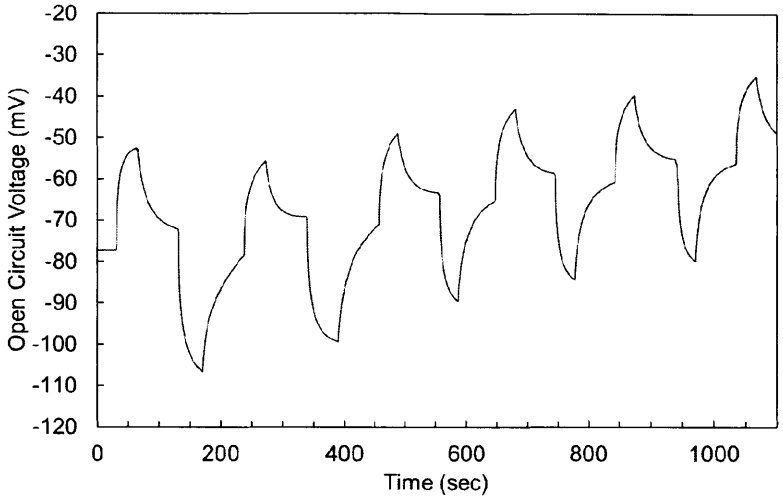

Figure 3-6: Open circuit voltage measured while bending the device in opposite directions at 0.17cm radius of curvature. Open circuit voltage peaks in alternating directions corresponding to each bending direction are shown.

3.4.2 Short circuit current

Short circuit current indicates the current signal with no load connected. This also demonstrates the maximum amount of current the device is able to generate at a given amount of bending. Figure 3-7 shows the measured short-circuit current as the device is bent with a radius of curvature of 2.0cm and then relaxed by releasing the bending forces. The bending and relaxation periods were 10seconds each. Bending induces a sharp rise in the current, suggesting the stress-driven Li^+ migration inside. When holding the bending at a fixed radius of curvature, the current signal quickly reaches a maximum beyond which it decays gradually. This decay is due to the cancellation between the externally applied bending stress and Li insertion/extraction induced stress in the electrodes. Specifically, externally applied bending creates tensile stress on one electrode and compressive on the other, generating a chemical potential difference that drives Li diffusion from the compressive to the tensile sides against the Li concentration gradient. At the same time, Li extraction from the compressed electrode and insertion into the tensed electrode attenuate both the compressive and

tensile stresses, corresponding to a reduced driving force for Li^+ diffusion and to the gradual current decay. The current signal vanishes when the chemical potential between the two electrodes vanishes. The full width at half maximum (time for peak current value to drop to half) was 3.0 second on average, which is two orders of magnitude greater than a typical piezoelectric device in similar geometry, promising the applicability of the device in the low frequency regime.[31]

Upon releasing the device from external bending force, Li insertion/extraction generated stress difference along with the Li concentration gradient in the electrodes serves as the driving force for the backward Li^+ migration, corresponding to a sharp current increase in the opposite direction. As Li^+ migration continues, the stress and concentration difference between the two electrodes drop, so as the driving force for Li^+ diffusion, leading to a reduced current signal. The current signal vanishes when the two electrodes recover to their original, isopotential state.

During the alternative bending experiment, the current signal follows similar manner to the one directional bending experiment, however, now exhibits the forward and backward current. As shown in Figure 3-8, The first peak in negative peak amplitude is followed by the positive peak from backward current. The third peak in positive peak is the result of bending the unit in the opposite direction, followed by its backward current. Similar to the one directional bending experiment, the full width at half maximum reaches up to 4.3 seconds.

As derived in Chapter 3-3, the amount of Lithium expected to transport with given amount of bending can be estimated from the amount of electrode material affected by bending. The amount of electrode material affected is computed based on the geometry with respect to the radius of curvature (R) and bending angle (Θ). The amount of silicon (N_{Si}, number of moles) is computed with respect to the thickness of the electrode (t), width of the device (w), density of silicon (ρ), and molar mass of silicon (m_{Si}).

$$N_{Si} = \frac{(t \times R\Theta \times w) \times \rho}{m_{Si}} \tag{3.4.1}$$

Since the composition in Li_xSi alloy is precisely known from the lithiation profile, we

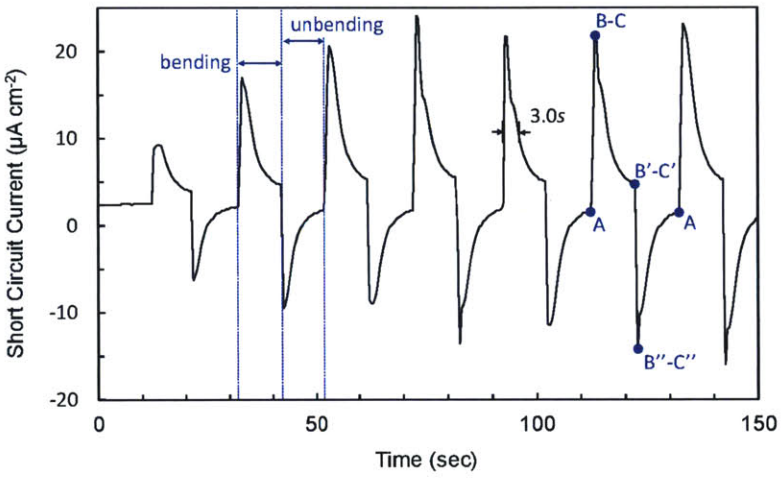

Figure 3-7a: Short circuit current density during bending tests. Bending was maintained at 2.0 mm radius of curvature with 10s intervals. The positive peaks correspond to the current during bending and negative peaks to the current during unbending. The points labeled in alphabet correspond to the geometries labeled in Figure 3-2a.

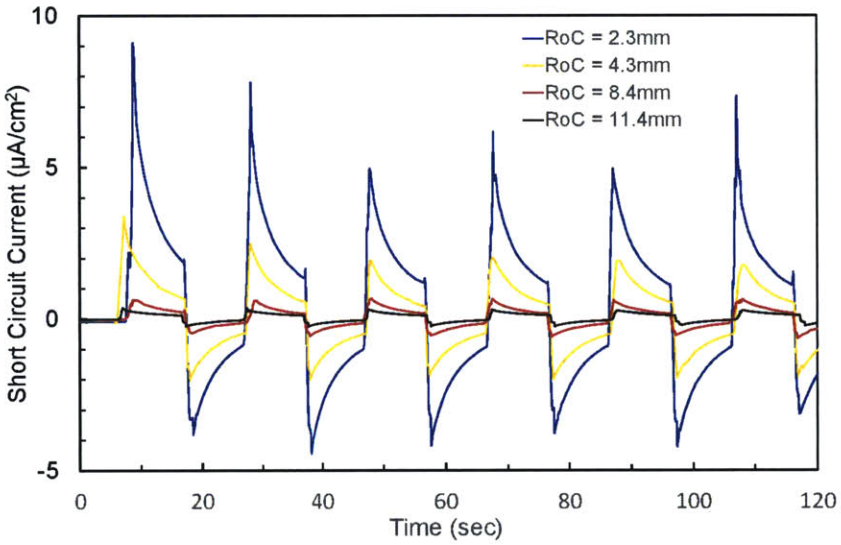

Figure 3-7b: Radii of curvature dependence on short circuit current.

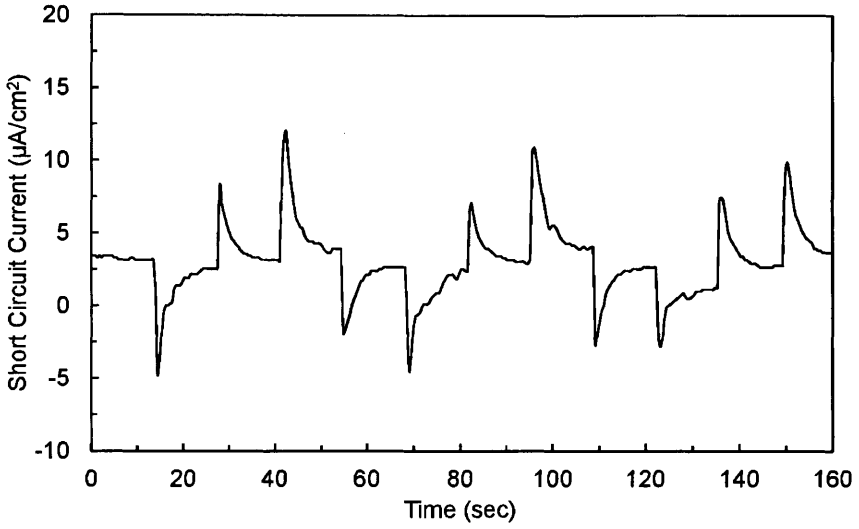

Figure 3-8: Short circuit current density during alternative bending

may obtain N_{Li} by simply multiplying the normalized alloy composition to N_{Si}. For our experiment performed in Figure 2-1, plugging in the following numbers results in the above equation results in $N_{Si} = 3.9\times10^{-7}$

$$(t = 75\text{nm},\ w = 2\text{cm},\ R = 0.2\text{cm},\ \Theta = 90°)$$

Since the thin film is lithiated to $Li_{3.1}Si$ composition, the number of moles of lithium in the affected area is $N_{Li} = 1.2\times10^{-6}$. The final thickness of the thin film is estimated assuming perpendicular volume expansion to the substrate direction, as observed in previous reports.[53] The volume expansion is estimated based on results of previous reports, resulting in 249nm $Li_{3.1}Si$ thin film.[53] This gives the one-side volume of the affected area to be $1.56 \times 10^{-5}cm^3$. This number may vary depending on the radii of curvature. Plugging this number in results in Li^+ ion migration is equivalent to $487\mu C$. On the other hand, the amount of Li^+ ions that migrate during each bending cycle is equivalent to the area under a current peak. In Figure 3-7a, the area under a peak is approximately $73\mu C$. Thus, the reversible lithium migration of $73\mu C$ is approximately 15% of the theoretically predicted amount.

It is worth noticing here that the composition change that occurs from bending the device is not large. Specifically, the thermodynamic amount of Lithium migration

(equivalent to 487μC) is approximately 5×10^{-9}moles. In terms of ratio, this is equivalent to 0.4% or the net change in composition of 0.013 out of 3.1. For instance, the expected composition of the compressed electrode after bending at 2mm radius of curvature is $Li_{3.087}Si$ and that of the tensed electrode $Li_{3.113}Si$.

The reduced generating capacity per cycle may be caused by "self-discharging", that is, the electrons diffuse out of the bent region to the nearby flat regions within the same Li_xSi electrode without going to the external circuit, which actually causes the flat regions to curve. Such self-discharging behavior is predicted to occur whenever there are unequal bending curvatures in the lateral direction (gradient in the bending curvature). This internal electrochemical dissipation by self-discharging can be greatly reduced by applying a uniform radius of curvature throughout the device.

3.4.3 Efficiency analysis

While the theoretical efficiency limit arises from the ratio of hydrostatic stress to deviatoric stress, the experimental energy harvesting efficiency of our device can be estimated from the following:

$$\eta \equiv \frac{U_{\text{electrical}}}{U_{\text{strain}}} = \frac{\int J^2 R dt}{\int_0^L \frac{EI(\omega'')^2 dx}{2}} \tag{3.4.2}$$

where J stands for current, R resistor, E the Young's modulus, and I the second moment of inertia. The maximum electrical energy output is achieved at an external load comparable to the internal resistance.

Figure 3-9 illustrates the voltage and current across external loads with varying load from 1Ω to 50,000Ω. The radius of curvature during bending was 9mm. The load that provides maximum power output is approximately 300Ω and is colored in light blue. This is significantly lower than many other types of mechanical energy harvesters, on the order of 10-100MΩ.[62][3] The nested figure demonstrates the Nyquist plot of the device and shows that the internal resistance of the device approximately matches with the load that provides the maximum power output. The strain energy

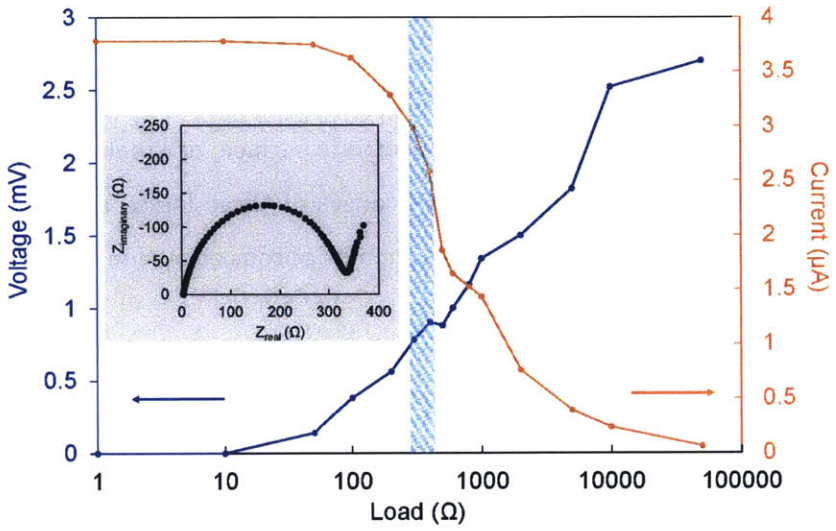

Figure 3-9: Voltage and current across external load varied from 1 to 50,000Ω. The external load that provides maximum power output is approximately 300Ω and is colored in light blue. The nested figure inside shows that the internal resistance of the device roughly matches the load that provides maximum power output.

stored during bending the device can be estimated as the following.

$$U_{\text{strain}} = \sum_{\text{component}} \int_0^L \frac{EI(\omega'')^2 dx}{2} = \sum_{\text{component}} \frac{\Theta EI}{2R} \tag{3.4.3}$$

Assuming a three layer (Li_xSi electrode - polymer separator - Li_xSi electrode) assembly, we obtain the estimated experimental efficiency of 0.62%. The Young's modulus of electrolyte soaked separator is directly measured and reported to be 0.35GPa in the literature.[56] The loss in efficiency may be understood from 1) dissipative modes in U_{strain} 2) resistive and kinetic loss in $U_{\text{electrical}}$. We have shown in the main text that only a fraction of the strain energy input is converted to electrical energy, due to the presence of the deviatoric stress tensor and also self-discharge between flat and non-flat regions. Contribution from vibration and frictional loss is also expected to reduce the efficiency despite a small amount.

Resistive and kinetic energy loss from is also expected. The presence of internal resistance brings resistive energy loss to the internal resistance. Also, as pointed out in

the main text, the amount of actual charge transferred per bending is estimated to be approximately 10% of the generating capacity. This may be due to various reasons including self-discharge to a non-bent region, SEI layer formation at the electrode surface, charge transfer resistance at the electrode surface, or kinetic limitations from slow Li^+ ion diffusion. In most cases, the causes of these losses may be engineered and optimized through various techniques such as porous electrode design or artificial SEI layer design.

3.4.4 Electrical energy output during repeated bending cycles

Figure 3-10 shows the data from two kinds of repetitive bending fatigue tests. In repeated open-circuit voltage tests, we observe that not only the peak height but also the background voltage are reduced over cycling, despite bent at moderate radius of curvature of 10mm. (Figure 3-10a) This is due to the damage accumulation in the electrodes. In open-circuit voltage measurements, lithium ions cannot migrate between the electrodes to relax the stresses developed in the electrodes. As a result, damages are accumulating in the electrodes in the form of pore formation, or even fracture. Since the films can no longer sustain the elastic stress, the peak heights decrease. In addition, it is expected that the electrode under repetitive tension exhibits different damage accumulation from that under repetitive compression. This difference results in the potential difference between the two electrodes and changes the background potential.

In repeated short-circuit current tests, in contrast, we observe no major degradation in the peak height with 4mm bending radius of curvature. The data in Fig. 3-10b shows reliable current generation during 1500 repeated bending cycles. The background current is slowly moving towards zero during cycling in a stable manner.

Repeated bending tests of 1500 cycles were performed at three different radii of curvature (3.6mm, 4.0mm and 11.4mm). Figure 3-11 illustrate the data. During the tests, we find that the background current (average current value between forward peak and backward peak) moves towards zero, as expected from chemical potential differences. This is true for 11.4mm and 4.0mm radii of curvature, but not true when

cycled at 3.6mm radius of curvature. During cycling at 3.6mm radius of curvature, the background current fluctuates and eventually decreases to -2μA from the original value of zero. The background current is expected to occur from inhomogeneous lithiation profile during sample preparation. The fluctuating and decreasing background current may indicate that plastic deformation accumulates on one electrode more severely than the other, causing the background current to fluctuate and eventually move out of equilibrium. With the current electrode design and packaging, we find from these durability tests that 4.0mm is the optimum radius of curvature, balancing between the power output and electrode stability

These fatigue stability test results indicate that the electrode materials maintain their homogeneity during cyclic loading of 1500 cycles. The reliable performance of the device during short-circuit fatigue test is enabled as the migrating lithium ions act as effective stress reliever in the electrode, much the same way as in Nabarro-Herring creep.[31] It might thus be possible to adapt our active mechanical-passive electrochemical (AMPE) fatigue tests as a diagnostic tool to characterize damage creation, repair and accumulation inside electrode materials, as a complementary technique to the electrochemically driven battery cycling testing paradigm that monitors voltage-induced mechanical strain (such as film curvature change).

We also performed the durability test while alternating the bending direction between positive and negative bending. We observe that the overall current peaks are lower than that obtained from single bending direction but with occasional unexpectedly high peaks, indicating unstable mechanical response. The fluctuation in average current is also more severe than the single bending direction. We observe that such instability eventually leads to reduced peak height after 1000 cycles despite at 4.0mm radius of curvature.

3.4.5 Effect of strain rate and bending frequency

Since the electricity generation is driven by Li^+ ion diffusion, the effect of bending rate and frequency can be understood based on the characteristic time scales of Li^+ ion diffusion. While there are time scales for mechanical equilibrium and diffusion

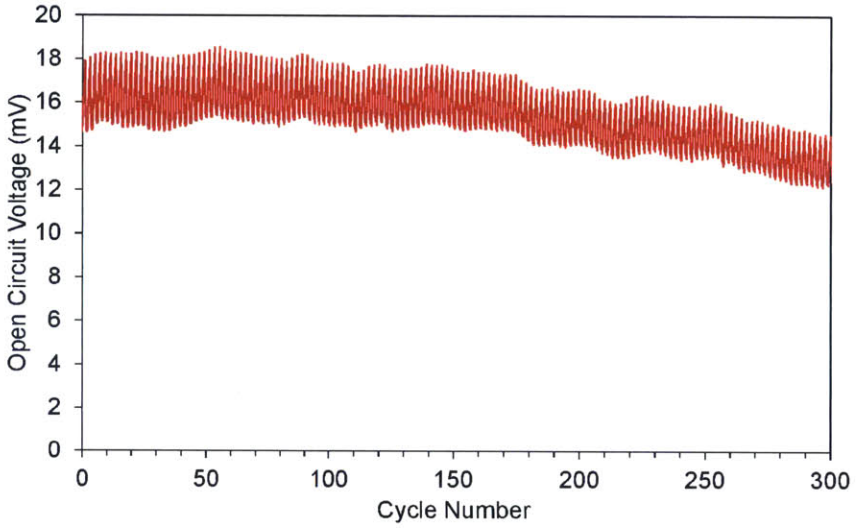

Figure 3-10a: The open-circuit voltage generated during repeated bending tests at 10 mm radius of curvature

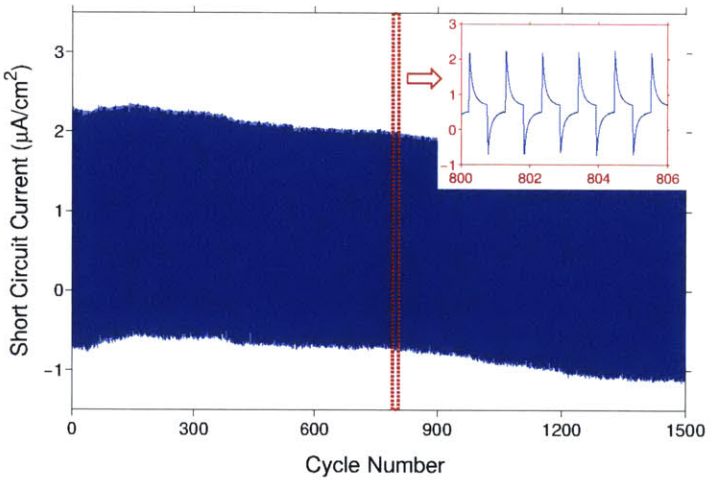

Figure 3-10b: Short-circuit current collected during repeated bending tests at 4.0mm radius of curvature. The nested figure shows the zoomed-in view of the 800th-807th bending cycle.

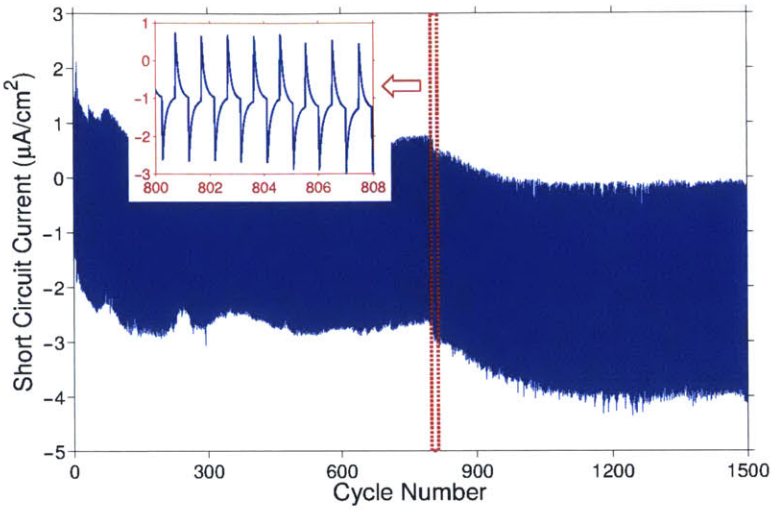

Figure 3-11a: Short circuit current density during 1500 bending and unbending cycles measured at 3.6mm radius of curvature The nested figure inside shows the zoomed-in view of the cycles between 800th and 807th bending.

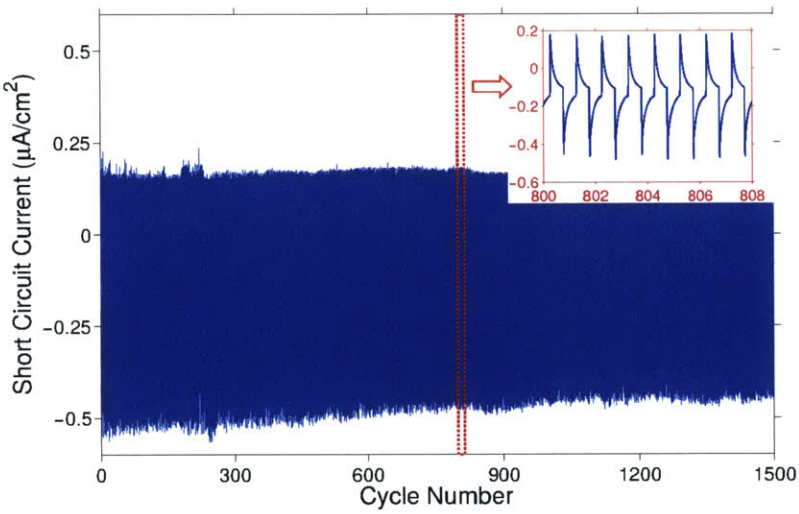

Figure 3-11b: Short circuit current density during 1500 bending and unbending cycles measured at 11.4mm radius of curvature The nested figure inside shows the zoomed-in view of the cycles between 800th and 807th bending.

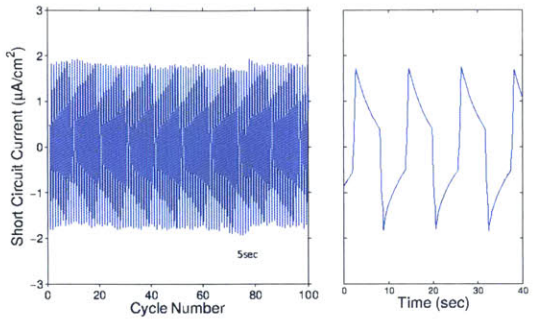

Figure 3-12a: Short circuit current density measured at 3.6mm radius of curvature, at strain rate of 0.35% s^{-1} and bending frequency of 0.07Hz.

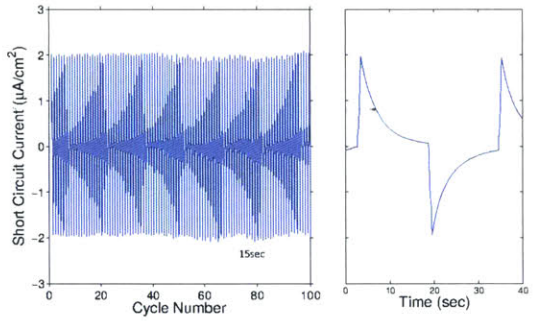

Figure 3-12b: Short circuit current density measured at 3.6mm radius of curvature, at strain rate of 0.35% s^{-1} and bending frequency of 0.2Hz.

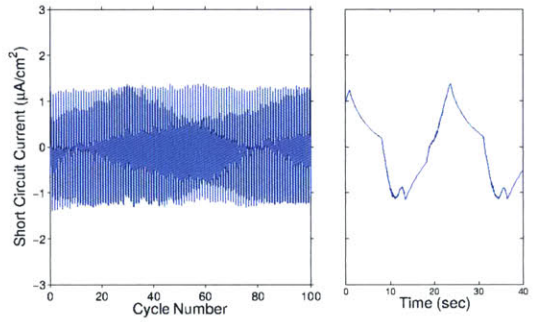

Figure 3-12c: Short circuit current density measured at 3.6mm radius of curvature, at strain rate of 0.07% s^{-1} and bending frequency of 0.2Hz.

equilibrium, the mechanical equilibrium in the elastic range is established very fast. Thus, potential bending rate effect comes from the competition between applied strain rate and diffusion rate. Using a typical value of $D_{Li} = 10^{-10}cm^2\ s^{-1}$ and letting 250nm be the characteristic diffusion distance, we estimate that the characteristic diffusion time is about 6 seconds. As long as strain rate exceeds Li^+ ion diffusion rate characterized by the width of the short circuit current signal, we observe identical current curves with similar full width at half maximum. If strain rate is slower, a current signal with extended width and reduced peak current is expected. In either case, the total energy output or repeatability is not expected to change due to the bending rate. Similarly, slow bending frequency would allow sufficient time for Li^+ ions to migrate between the electrodes and does not affect the output energy.

These explanations are demonstrated experimentally while bending at 4.0mm radius of curvature at different bending frequency and speed. Figure 3-12 illustrate the results. In order for clear comparison, the background current was removed. When the strain rate is maintained at 0.35% s^{-1} and bending frequency is varied from 0.2Hz to 0.07Hz, we do not observe any noticeable change in short circuit current peak height or change in durability during 100 cycles. When the bending frequency is maintained at 0.2Hz and strain rate is varied from 0.35% s^{-1} to 0.07% s^{-1}, we observe that the short circuit current peak shape widens during bending and peak height decreases. As mentioned earlier, however, the total amount of charge transferred during each bending cycle remains almost identical.

If bent at a frequency so high that Li^+ ions do not have sufficient time to migrate between electrodes, the electrodes are not able to relieve stress by lithium insertion/extraction and will eventually fail by fatigue. This is in part equivalent to low temperature condition in Nabarro-Herring creep. This frequency, however, far exceeds the human activity timescale. The device is therefore not well suited for vibrational energy harvesting at high frequency ($\gg$ 100Hz).

3.5 Comparison to existing energy harvesters

The energy output generated from the device in general exhibits a greater amount of current and less voltage when compared to the ceramic piezoelectric generators.

Table 3-1 shows the comparison of peak power and energy output operated at 0.3Hz frequency for known piezoelectric generators and our device. The piezoelectric generators cited in Table 3-1 have similar geometry to our device and the difference in energy output comes mainly from the material properties. The comparison is based on the area of the thin film generators without considering film thickness, as the microstructure of the materials as well as the effect of thickness on performance differ significantly among the reported generators. In Table 3-1, PMN-PT refers to (1-x)Pb($Mg_{1/3}Nb_{2/3}$)O_3 - $x$$PbTiO_3$ and is a single crystalline thin film, while $BaTiO_3$ is a nanoparticle composite.[8, 64] KNLN refers to 072($K_{0.480}Na_{0.535}$)NbO_3 - 0.28$LiNbO_3$ and is a nanoparticle composite.[66] Peak power is considered to be the direct product of short circuit current and open circuit voltage. The energy output at 0.3Hz is calculated, assuming that the average peak width (full width at half maximum) of piezoelectric generators is 100 millisecond and that the peak width of our device is 3 seconds. As shown in Table 3-1, the peak power for our device is in general less than those of piezoelectric generators. Nevertheless, when operated under low frequency such as 0.3Hz, the amount of energy generated per second is comparable to the best non-lead containing piezoelectric generators in the same form factor; our device outperforms those made of $BaTiO_3$ or KNLN by at least one order of magnitude. The PMN-PT based generators and ZnO nanowire generators outperform our device; nevertheless, these devices are elaborately optimized.[65] PMN-PT generators consist of 20μm thick single crystalline thin film, grown and processed from an ingot of the material and sapphire substrate. The ZnO nanowire generators were optimized by coating the surface with layer-by-layer self-assembled polymer layer. Considering that both generators have gone through a significant amount of optimization, our device, with further optimization in material selection and architecture design, holds promise as an efficient energy harvester at low frequencies.

3.6 Conclusion

We have developed a novel type of mechanical energy harvester based on the fact that lithium ions have finite size (14.95Å^3), and thus would migrate across an electrolyte membrane under a pressure difference - akin to reverse osmosis in seawater desalination. But because lithium ions carry $+e$ charge, it would drive electron flow in the outer circuit, same as how a typical battery would work. The device achieves long current pulse duration, which has not been achieved by other types of mechanical energy harvesting devices. Due to this characteristic, the device exhibits higher average energy output than most other piezoelectric generators when operating at low frequencies. The analysis in this work also opens avenues for optimizing electrochemical devices coupled to mechanical stress for sensing and actuation, as well as the development of active mechanical-passive electrochemical (AMPE) tests as an alternative diagnostic protocol to study damage creation and accumulation in electrochemomechanically active solids.

Chapter 4

Timescale tunability in electrochemically driven mechanical energy harvesting

The design of an ideal mechanical energy harvester essentially involves the understanding of the motion the harvester targets to harvest. For high frequency motion harvesting, a rapid kinetic response to the mechanical input is desired. Such rapid responses are often characterized by sharp electrical current pulse with high peak amplitude. The duration of the electric current signal does not matter, as long as the duration of current signal is shorter than or equal to the duration of the mechanical input period. If the current lasts longer than the duration of mechanical input, the current will not be harvested. For low frequency motion harvesting, on the other hand, we may design the energy harvester to generate electric current for sufficiently long time, in order to maximize the electrical energy per unit of mechanical energy input. In other words, an ideal mechanical energy harvester in the low frequency regime may harvest a specifically targeted frequency motion to maximize its efficiency. This is in parallel to the notion that instantaneous power output, most often used in piezoelectric generator community, does not necessarily reflect the energy generation capacity over time, unless the frequency of the mechanical energy input is matched with that of the harvester's frequency. One measure for a harvester's frequency tunability may

be whether it is possible to tune the width of electric current pulse generated by the harvester.

The ability to tune the electric current duration, however, has not been possible with the conventional choices of mechanical energy harvesters such as piezoelectric generators or triboelectric generators. The current peaks generated by these two types of generators last for less than 100msec, making them ideal for harvesting high frequency motion over 10Hz.[67] Such high frequency motions are present in various home appliance machines including washing machines or refrigerators. Such short peak duration is the direct consequence of the piezoelectric or triboelectric effect and has not yet been tunable. Piezoelectric effect generates electric current from induced dipole moment within a crystalline unit cell, as a cation vibrates within a unit cell. The atomic vibration frequency is on the order of 10^{13}Hz, much higher than that of typical everyday motion.[38] Similarly, triboelectric generators rely on surface charge transfer between dissimilar materials and electrostatic induction. The time it takes for surface charges to transfer and electron clouds to re-distribute due to induction is considered to be instantaneous and indeed experimental observations reveal shorter peak widths for triboelectric generators than that of piezoelectric generators.[8, 68] Efforts to harvest motions with a spectrum of frequency has been made by engineering a bridge structure made of piezoelectric materials.[69] The structure provides increased band of frequency to be harvested, nevertheless, is still limited in motions with frequency above 10Hz and in device design.

In this chapter, we demonstrate the timescale tunability in an electrochemically driven mechanical energy harvester and provide a theoretical understanding based on the kinetic processes present in the device. The theoretical framework for designing an energy harvester targeted for specific low frequency motions will also be presented. This capability is first demonstrated among various types of mechanical energy harvesters and is expected to broaden the optimization space of mechanical energy harvesters, especially in the low frequency regime including everyday human motions.

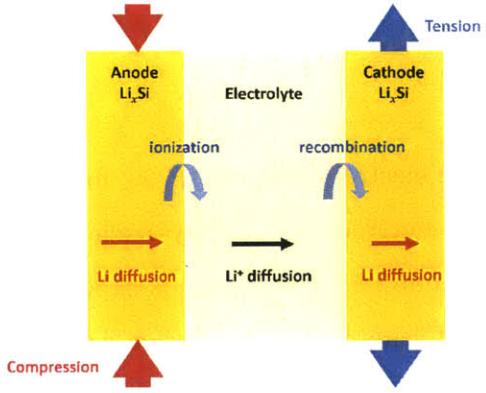

Figure 4-1: Kinetic processes involved in the energy harvester. In large, there are lithium atom diffusion inside the electrode, lithium ion diffusion in the electrolyte and charge transfer reaction at the electrode-electrolyte interface. The electron transport via external circuit is not explicitly drawn. These kinetic processes are also affected by the compressive and tensile stresses acting on the electrodes.

4.1 Kinetics processes in electrochemically driven mechanical energy harvesting

The electric current peak width, as briefly mentioned in the chapter introduction, holds the key to optimizing the harvester in terms of targeted frequency motion harvesting. This quantity is a complex manifestation of the kinetic processes present in the device and is likely dominated by the slowest kinetic process. In large, the major kinetic processes present in electrochemically driven mechanical harvesting are atomic lithium diffusion inside Li_xSi electrodes, charge transfer reaction at the interface between electrode and electrolyte, and Li^+ ion diffusion inside the electrolyte layer. Each physical process may also be affected by the stress state acting on the electrode or on electrode surface. The processes are illustrated in Figure 4-1. It is noted that the kinetics of all three processes can, in principle, be tuned significantly. In the following subsections, I will introduce and examine each kinetic process.

4.1.1 Stress-driven non-linear Li diffusion in electrochemical alloys

Lithium diffusion inside the electrode may be in the form of lithium ion diffusion or atomic lithium diffusion. In electrochemical alloys such as Li_xSi, the material behaves as a metallic compound and atomic Li diffusion is expected to occur. In ionic solids such as Li_xCoO_2, Li^+ ion diffusion and hole diffusion occur separately and need to be taken account explicitly. Such treatment involving Li^+ diffusion and polaron hopping has been studied in Li-ion battery community.[70, 71] In this thesis, I limit our focus and derivation to atomic lithium diffusion in electrochemical alloys alone.

As briefly mentioned in Chapter 2, the diffusion of non-dilute species in ideal binary compounds follows the Fick's law. When other diffusion potentials are present such as a hydrostatic pressure P acting on the material, the flux of a species i in a binary alloy can be expressed as the following.

$$j_{\mathrm{i}} = -D_{\mathrm{i}}\nabla c_{\mathrm{i}} - c_{\mathrm{i}}\frac{D_{\mathrm{i}}\Omega_{\mathrm{i}}}{kT}\nabla P \tag{4.1.1}$$

where Ω_i refers to the volume occupied by a species i. In amorphous Li_xSi alloy, insertion or removal of lithium atoms will cause volume change equivalent to the volume occupied by lithium. If the volume change is sufficiently small, as noted in Chapter 3.4.2, this volume change can be expressed in terms of a hydrostatic strain equivalent to $\frac{c-c_0}{c_0}$ where c_0 and c denote the original lithium concentration and lithium concentration after stress is applied. The flux of lithium after bending is then

$$j_{\mathrm{Li}} = -D_{\mathrm{Li}}\nabla c - c\frac{D_{\mathrm{Li}}\Omega_{\mathrm{Li}}}{kT}\nabla(P_{\mathrm{ext}} + B\Omega_{\mathrm{Li}}(c - c_0)) \tag{4.1.2}$$

where P_{ext} and B refer to the externally applied hydostatic pressure and bulk modulus, respectively. The hydrostatic stress acting on the electrode consists of a constant stress P_{ext} applied by bending and the change in stress $B(c - c_0)$ as the material adjusts lithium concentration. From here, the subscript Li from c_{Li}, D_{Li}, and Ω_{Li} are omitted for visual clarity and the symbols indicate those of lithium unless otherwise

specified. Since the divergence of a flux equals the net change in concentration, we may expand and organize as the following.

$$\begin{aligned}\frac{\partial c}{\partial t} &= -\nabla \cdot j = -\nabla \cdot \left[-D\nabla c - c\frac{D\Omega_{\mathrm{Li}}}{kT}\nabla(P_{\mathrm{ext}} + B\Omega_{\mathrm{Li}}(c - c_0))\right] \\ &= D\nabla^2 c + \frac{D\Omega_{\mathrm{Li}}^2 B}{kT}\nabla \cdot (c\nabla c) \\ &= D\nabla^2 c + \frac{D\Omega_{\mathrm{Li}}^2 B}{kT}\left[c\nabla^2 c + (\nabla c)^2\right] \\ &= \left(D + \frac{D\Omega_{\mathrm{Li}}^2 Bc}{kT}\right)\nabla^2 c + \frac{D\Omega_{\mathrm{Li}}^2 B}{kT}(\nabla c)^2\end{aligned} \tag{4.1.3}$$

In the derivation, it is assumed that D_{Li} is independent of composition for the composition range we are considering, since the change in composition is much smaller than the absolute composition. According to the estimation by mechanics analysis in Chapter 3.3, the expected change in composition is approximately 0.4%, or equivalently, between $Li_{3.09}Si$ and $Li_{3.11}Si$. While the first term in Eq. 4.1.3 represents the Fick's law diffusion with modified effective diffusion coefficient, the second term represents the non-linearity in the stress-driven diffusion of Li.

The non-linearity term in flux expression ($\frac{D\Omega_{\mathrm{Li}}^2 B}{kT}(\nabla c)^2$) is always positive regardless of the sign of the change in concentration. The effect of this term on the kinetics is expected to be one-directional; that is, the kinetics during bending and unbending will be different.

4.1.2 Butler-Volmer model for charge transfer kinetics

The charge transfer reaction that takes place on the surface of each electrode, $Li \leftrightarrow Li^+ + e^-$, follows the phenomenological description by Butler-Volmer model. The electrodes at first are in equilibrium with the electrolyte. The initial overpotential applied by stress can be expressed as the following.

$$\eta = \frac{\sigma_{\mathrm{hydro}}\Omega_{\mathrm{Li}}}{e} \tag{4.1.4}$$

As diffusion continues, the overpotential will not be constant over the thickness of the electrode, and will be a continuous function of composition. Assuming that the charge transfer coefficient is one half, we may write the Butler Volmer kinetics on the surface of one electrode.

$$j = j_0 \left[exp^{\frac{\Omega_{Li}(P_{ext}+B\Omega_{Li}(c-c_0))}{2kT}} - exp^{\frac{-\Omega_{Li}(P_{ext}+B\Omega_{Li}(c-c_0))}{2kT}} \right] \tag{4.1.5}$$

Expanding the exponential and grouping the constant terms, we obtain the following:

$$j = j_0 \left[a \times exp^{Kc} - a^{-1} exp^{-Kc} \right] \tag{4.1.6}$$

where a stands for $exp^{\frac{\Omega P}{2kT}}$ and K stands for $\frac{B\Omega_{Li}^2}{2kT}$.

Assuming no self-discharge (recombination of Li^+ and e^- elsewhere), the total number of electrons involved in current generation is equal to the number of lithium atoms migrating from the electrode. Thus, the following boundary condition holds.

$$-Ad_0 \times \frac{\partial c}{\partial t} = \frac{dN_{\text{Li+ (electrolyte)}}}{dt} = A \times j \tag{4.1.7}$$

where A and d_0 stand for the electrode-electrolyte interface area and thickness of the electrode. Inserting the Butler-Volmer expression for flux j and simplifying the terms yields the following.

$$\frac{\partial c}{\partial t} = -\frac{j_0}{d_0} \left[a \times exp^{Kc} - a^{-1} exp^{-Kc} \right] \tag{4.1.8}$$

As shown in chapter 3, the overpotential applied by stress in our device is relatively small. With 2mm radius of curvature, the expected voltage difference between the two electrodes is approximately 25mV. This indicates that the overpotential on one electrode is approximately 12.5mV. This is comparable to or smaller than the thermal energy at room temperature (kT = 24mV). As current passes on, stress will be mitigated by the departure/arrival of lithium into the electrode, and this overpotential will be decreased even further. In the small stress limit, the expression can be

expanded via Taylor expansion to yield the following expression.

$$\frac{\partial c}{\partial t} \approx -\frac{j_0}{d_0}\left(aKc + a^{-1}Kc\right) \approx -j_0\overline{K}c + K' \tag{4.1.9}$$

Since the time derivative of concentration directly depends on concentration itself, the solution to this ordinary differential equation will have exponential form of solution. Physical process following this behavior will exhibit the linear behavior between electric current output and time.

4.1.3 Lithium ion diffusion inside electrolyte

The mobility of lithium ion in electrolyte is often expressed as conductivity instead of diffusivity due to the charge carrying lithium ion. In order to maintain charge neutrality in the electrolyte, we may safely assume that the number of lithium ions remain constant during the operation of the device. In other words, the number of lithium ions ejected from one electrode will be identical to that injected into the other electrode. With this assumption, we can assume that the kinetics of lithium ions inside the electrolyte remains almost unchanged during the operation of the electrolyte.

For typical choice of lithium ion battery electrolyte (1:1 volume ratio mixture of ethylene carbonate and ethyl-methyl carbonate with 1M $LiPF_6$, also the electrolyte used throughout this thesis), the conductivity is measured to be approximately 10^{-2} S/cm.[72] Assuming little or no ion-ion interaction, we may estimate how long it will take for a lithium ion to drift the entire thickness of the electrolyte. In an ionic medium, the conductivity is expressed as the product of charge per carrier (e), carrier density (n) and drift mobility (ν).

$$\sigma = en\nu \tag{4.1.10}$$

Since this expression involves conductivity contributed by both anionic and cationic species, the conductivity of cations can be written with the cationic transference

number (t_c). The transference number varies between 0 and 1, and is assumed to be 0.4 here.

$$\sigma_c = \sigma \times t_c = e n_c \nu_c \tag{4.1.11}$$

Given the values for the electrolyte we use, we may estimate the drift mobility of Li^+ ions in the electrolyte.

$$\begin{aligned} \nu_c = \frac{\sigma_c}{en} &= \frac{10^{-2}}{\Omega\text{cm}} \quad \frac{0.4}{1.6 \times 10^{-19} C} \quad \frac{1000\text{cm}^3}{6.02 \times 10^{23} V \cdot s} \\ &\approx 4.16 \times 10^{-5} \frac{\text{cm}^2}{Vs} \end{aligned} \tag{4.1.12}$$

With the Einstein relation for charged particles, Li^+ diffusivity in electrolyte can be estimated as the following.

$$\begin{aligned} D_{\text{Li}} &= \frac{\nu_{\text{Li}} kT}{e} \\ &= 1.04 \times 10^{-6} \text{cm}^2/s \end{aligned} \tag{4.1.13}$$

It is noted here that Li^+ diffusivity is several orders of magnitude larger than that of Li atom diffusion in the electrode material and is safely assumed to be much faster than the other two kinetic processes.

4.1.4 Rate limiting kinetic process

The overall kinetics of a chemical reaction is often dominated by the slowest kinetic process called rate limiting step. The overall kinetic behavior will essentially follow that of rate limiting step.

If the device's kinetics is limited by diffusion, we will observe that the overall kinetics following the diffusion behavior. When bending is applied, lithium migration continues until the potential difference between the two electrodes eventually reaches zero. As the driving force for diffusion during bending decreases over some time, the non-linearity disappears. This indicates that the concentration profile over time will

be following Fick's law behavior or equivalently power-law behavior as mentioned in Chapter 2.3.2.

If charge transfer kinetics is the slowest, we will observe the kinetics of Butler Volmer model in the entire device's kinetics. In the small overpotential limit, equivalent to the temporal region after sufficient amount of current output, Butler Volmer kinetics will be manifested by the exponential behavior. This behavior is apparent if the semi-log plot with logscale current output axis and linear time axis.

4.2 Interpretation of the experimental data

As mentioned in previous section, the rate limiting kinetic process determines the overall kinetics of the current generation. We may identify which kinetic process dominates of the three different types via examining the behavior of the experimentally measured current output. In order for this purpose, the device was cycled between bending it for 600 seconds and unbending it for 600 seconds. Figure 4-2 illustrates the data obtained during the cycling, for an energy harvester with 400nm $Li_{3.1}Si$ electrodes.

To assess whether the limiting kinetics occurs from charge transfer reaction or solid state diffusion, a representative peak in Figure 4-2 is plotted using linear scale (Figure 4-3a), log-scale only in y axis (Figure 4-3b) and log-scale in both x and y axes (Figure 4-3c). In Figure 4-3c with log-log scale, we find linear relation arising after the initial 1 second, suggesting the diffusion limited kinetics. It is noted here that the current generation rate is almost constant between 10^{-2} second and 1 second as observed in Figure 4-3c. This is due to the finite amount of time taken to bend the device via servo motor. The servo motor described in Chapter 3 had a strain rate of $0.35\%s^{-1}$, and it took approximately 1 second for the motor to bend the device. If the electric current generation rate is faster than that, it may not have been measured in this experiment since strain rate limited the kinetic rate. Thus, the constant current rate between 10^{-2} second and 1 second will not be considered in the analysis. Also, after approximately 300 seconds, we observe the slope in linear

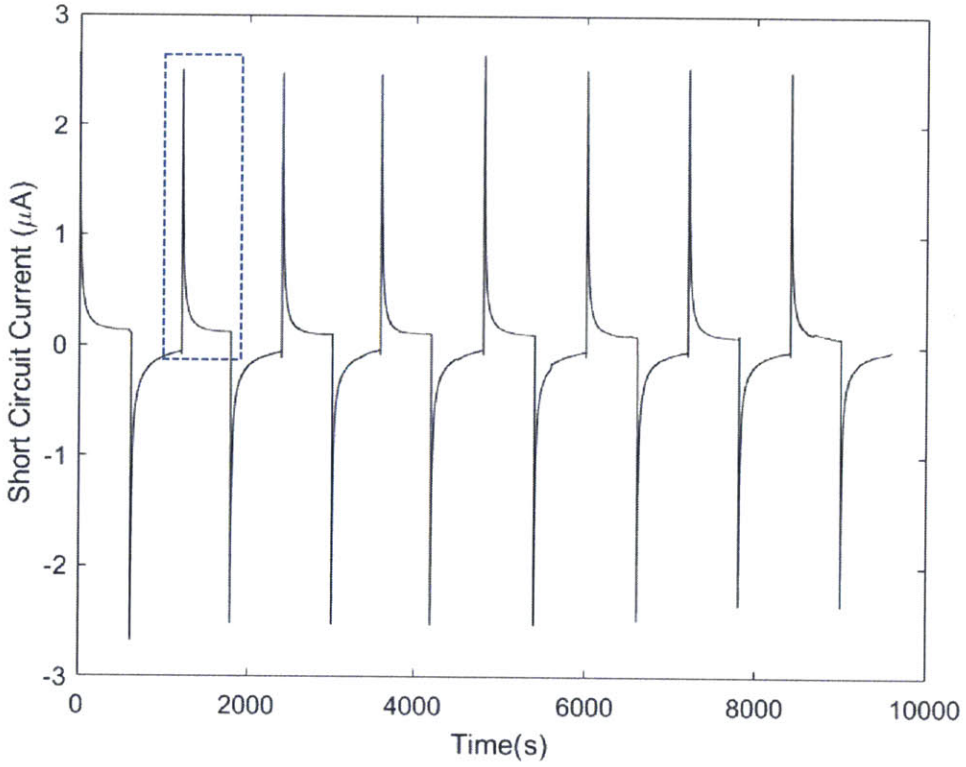

Figure 4-2: Short circuit current during repeated bending and unbending for 600 seconds, respectively. A representative peak is boxed in blue.

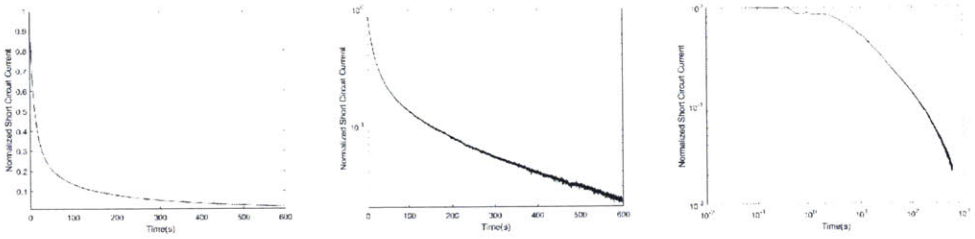

(a) Linear x and y axis (b) Log-scale y axis (c) Log-scale x and y axis

Figure 4-3: Analysis of a representative peak during bending an harvester made of 400nm electrodes for 600s.

behavior in Figure 4-2c decreasing further. This may be caused by the depletion of excess lithium concentration to be transferred, resulting in decreased current rate. Thus, this region will also be disregarded in the analysis.

4.3 1D model analysis

In order to understand the kinetics and timescale observed during open circuit potential measurement and short circuit current measurement, a simplified 1D model is constructed. The model consists of a single electrode interfacing with electrolyte on one end. Stress-dependent diffusion and Butler Volmer kinetics will be employed in the model, along with finite thickness of capacitive dielectric layer at the interface between electrode and electrolyte.

4.3.1 Model construction

Short circuit current

In order to understand the kinetics better, 1D model is constructed based on Li diffusion inside electrode and charge transfer reaction as the boundary condition (Figure 4-4). In the model, lithium is diffusing only in x direction, across the thickness of the electrode. Diffusion into the other directions is assumed to be negligible, based on the premise that diffusion into the other directions is much slower and longer. The ohmic resistance inside the electrode and external circuit is assumed negligible;

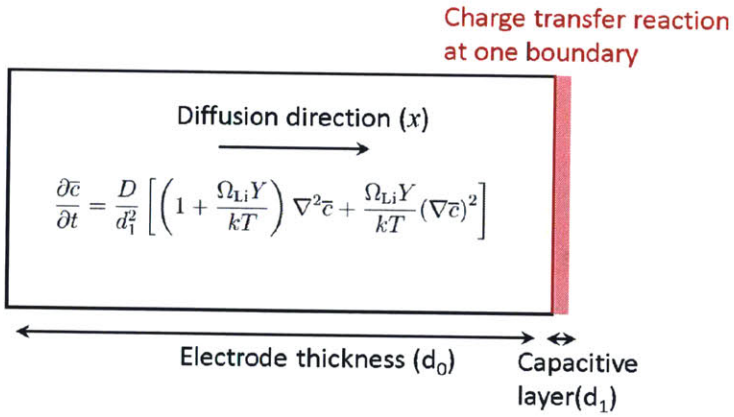

Figure 4-4: 1D model diffusion model with Butler Volmer type boundary condition on one end.

the electrons generated by charge transfer reaction are assumed to flow at an infinite rate, without the possibility of accumulation at the surface. This effect also causes the double layer capacitive charging, which is assumed to be effectively zero with sufficiently fast diffusion inside electrolyte.

For robust model construction, the parameters in the following diffusion equation derived in 4-1 are non-dimensionalized.

$$\frac{\partial c}{\partial t} = \left(D + \frac{D\Omega_{\mathrm{Li}}^2 Bc}{kT}\right)\nabla^2 c + \frac{D\Omega_{\mathrm{Li}}^2 Bc}{kT}(\nabla c)^2 \tag{4.3.1}$$

We can write concentration (c) as the sum of initial concentration (c_0) and the change in concentration (Δc). As observed in mechanics analysis (Chapter 3.3) and experimental data (Chapter 3.4), the change in concentration is much smaller than the initial concentration ($c_0 \gg \Delta c$). We will introduce a normalized concentration ($\overline{c} \equiv \Delta c / c_0$). We then normalize the distance variable x with normalized distance $\overline{x}$ such that $x = \overline{x} d_1$ where d_1 indicates the electrode thickness. Writing the diffusion equation in terms of the normalized variables, we obtain the following expression.

$$\frac{\partial \overline{c}}{\partial t} = \frac{D}{{d_1}^2}\left(1 + \frac{\Omega_{\mathrm{Li}}^2 Bc_0}{kT}\right)\nabla^2 \overline{c} + \frac{D}{{d_0}^2}\frac{\Omega_{\mathrm{Li}}^2 B{c_0}^2}{kT}(\nabla \overline{c})^2 \tag{4.3.2}$$

On one end of the electrode, sufficiently fast charge transfer reaction in the form of Butler Volmer kinetics is imposed. The definitions of a and K are the same as those defined in (4.1.6).

$$\frac{\partial c}{\partial t} = -\frac{j_0}{d_0}\left[a \times exp^{Kc} - a^{-1}exp^{-Kc}\right] \tag{4.3.3}$$

Open circuit current

While capacitive double layer charging is assumed to be negligible during short circuit current measurement, measuring open circuit potential results in significant amount of capacitive double layer charging, since charges are not allowed to migrate to the other electrodes. Thus, we introduce parameters for capacitive double layer charging in this part, including its thickness (d_1) and dielectric constant (ϵ). The charge density stored in the capacitance is denoted as σ.

In terms of physical insight, each migrating lithium atom undergoes charge transfer reaction at the electrode-electrolyte interface and dissolves into the electrolyte, leaving an electron at the electrode surface. Unlike in short circuit current case where electrons are driven to the other electrode via electric potential difference and connected external circuit, the circuit is not connected for open circuit measurement. Thus, the electron stays at the interface, building a charge density σ. This charge density attracts the oppositely charged ions near the surface, building a double layer.

The measured open circuit potential is, by definition, the difference in lithium chemical potential between the compressed and tensed electrode (Figure 4-5). Migration of lithium from one electrode to the other continues until the electric potential stored inside the capacitance cancels out the lithium chemical potential difference. In other words, the measured open circuit potential rises upon bending the device, until an equilibrium potential difference is reached. The stored charge density can be expressed in terms of lithium concentration.

$$\sigma = \frac{e(c_0 - c)}{A} \tag{4.3.4}$$

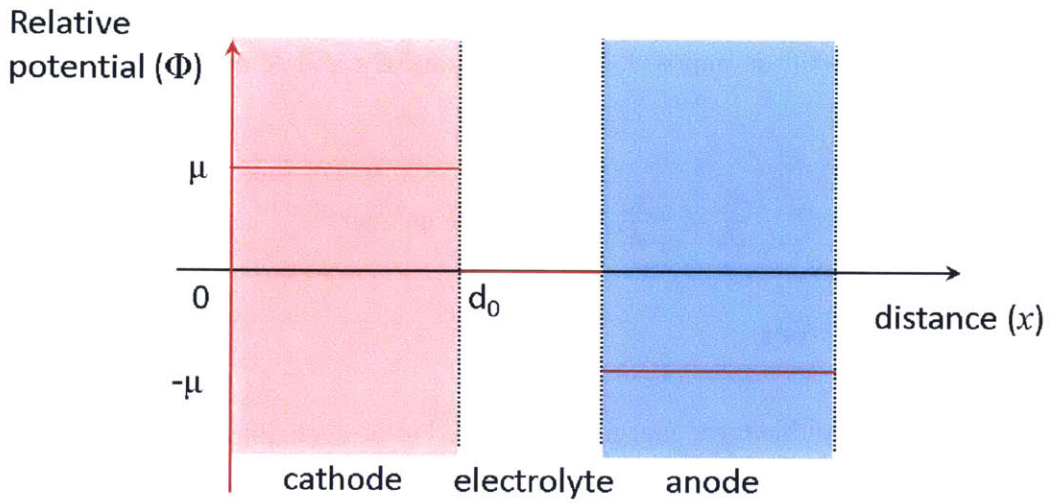

Figure 4-5: Relative potential diagram for the two electrodes sandwiching an electrolyte layer. The potential axis is normalized with respect to the lithium potential inside the electrolyte. Although greatly exaggerated inside the figure, the electrodes are assumed very thin.

The electric potential stored in the double layer is then

$$\phi = \frac{\sigma}{\epsilon} d_1 = \frac{e(c - c_0)}{A\epsilon} d_1 \tag{4.3.5}$$

In the model, while the diffusion model remains identical to the short circuit current case, the charge transfer model gets modified slightly with the insertion of double layer capacitance in the model. The overpotential now includes the electric potential introduced earlier, along with the stress driven lithium chemical potential difference.

$$j = j_0 \left(e^{\mu - \frac{\sigma}{\epsilon} d_2} - e^{-\mu + \frac{\sigma}{\epsilon} d_2} \right) \tag{4.3.6}$$

4.3.2 Numerical Solution

Short circuit current

The constructed model is evaluated numerically via Runge-Kutta numerical scheme.[73] The results obtained from numerically solving the diffusion equation (4.3.3) are il-

lustrated in Figure 4-6. The figure captures the fast decaying characteristics of the current profile observed in Figure 4-2. Plotting the current in semi-log and log-log scales also show linear behavior in the log-log scale, as expected and observed from the experimental output in Figure 4-3. In the modeled current profile, varied electric current is observed between between 10^{-2} seconds and 1 second, unlike in the experimental output (Figure 4-3c). The non-linearity between this period is manifested by the changing slopes and indicates that the stress-driven driving force is significant during this time. The constant linearity between 1 second and 100 second indicates that diffusion may be driven by mainly by chemical potential gradient. This can be understood more clearly in Figure 4-6.

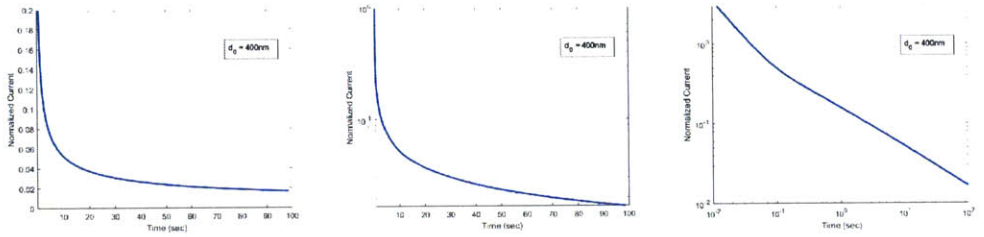

(a) Linear x and y axis (b) Log-scale y axis (c) Log-scale x and y axis

Figure 4-6: Numerically solved diffusion equation in linear, semi-log and log-log scales. 400nm electrodes are modeled for 100s with diffusivity of 10^{-12}cm^2/s. We observe clear linear behavior in log-log scale after 1 seconds.

Figure 4-7 illustrates the modeled concentration profile over time. As soon as stress is applied, charge transfer reaction occurs at the electrode interface from the stress driven overpotential. This causes quick lithium depletion near the surface. During the first second after stress is applied, a significant amount of lithium dissolved into the electrolyte. This quickly depletion near the surface causes a significant chemical potential gradient inside the electrode. As the amount of lithium diffusion continues to increase, the stress-driven term in the diffusion equation decays and the linear diffusion follows. This transition is observed to occur before the first second in Figure 4-5c. It is also noted that the amount of charge transfer during the first second and that during the next 9 seconds are approximately similar, indicating a considerably smaller current generation rate. As the rate becomes dominated more and more by

Fick's law diffusion, the rate slows down via power law as shown in Figure 4-6c. This is well observed in Figure 4-6. The area between 'Time = 10sec' curve and 'Time = 50sec' curve indicates the total amount of electric current generation. This is smaller than that generated within the first ten seconds. Similarly, the rate continues to decay as electrode diffusion limits the overall reaction rate further.

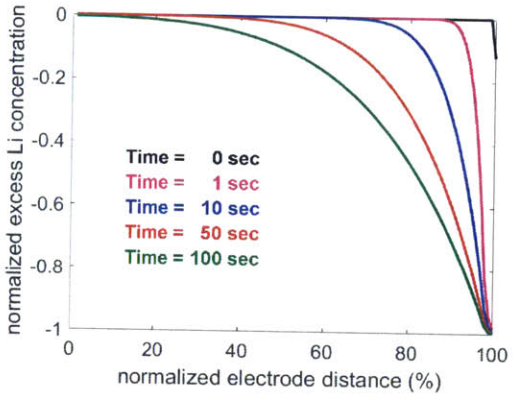

Figure 4-7: The modeled concentration profile inside compressed electrode over time, during a short circuit current measurement.

Open circuit voltage

Figure 4-8 illustrates the modeled open circuit voltage profile. Voltage first increases by a significant portion within the first few seconds, and the increasing rate decays over time until a voltage plateau is reached. This ratcheting behavior was observed experimentally and was depicted in Figure 3-4b. The modeled behavior agrees very well with experimentally observed behavior, except for the behavior during the first few second. Similar to the case in short circuit current measurement, this is understood in terms of the servo motor speed limited kinetics.

Figure 4-9 illustrates the role of electrode diffusion in the ratcheting behavior of open circuit potential. When the stress is applied to the electrode, charge transfer reaction immediately follows at the electrode surface. This time, however, electrons do not migrate due to open circuit and charge the double layer. As the electric potential charged in the capacitance equals the chemical potential difference imposed by stress, lithium dissolution into electrolyte stops. The concentration profile, at this point,

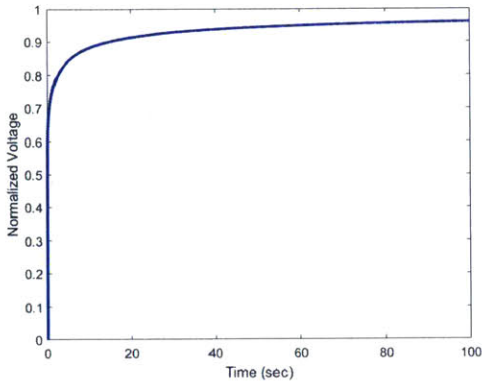

Figure 4-8: The modeled open circuit potential over time. The computed values arise from a single electrode, however, the experimentally measured voltages are expected to be twice the values observed from a single electrode.

is shown in dark brown. Lithium concentration gradient builds inside the electrode and triggers lithium migration within the electrode. Over time, lithium concentration slowly equilibrates into a constant value. The open circuit voltage which measures the difference in lithium chemical potential at the electrode and electrolyte surface increases along with lithium diffusion, as shown in Figure 4-9.

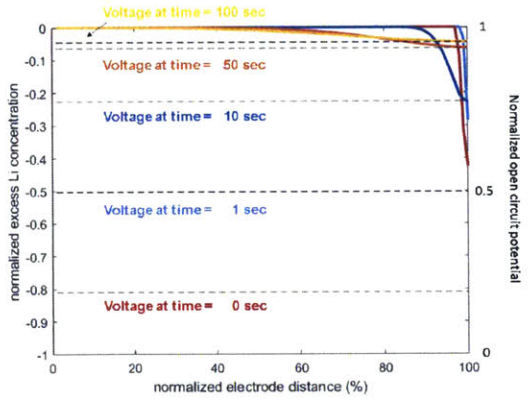

Figure 4-9: The modeled concentration profile inside the electrode during open circuit potential measurement over time. The initially introduced large lithium concentration gradient decreases by lithium diffusion, increasing the open circuit potential. The rate of voltage increase decreases as lithium concentration gradient decreases.

4.3.3 Experimental validation

In order to confirm the diffusion limited kinetics, we performed identical bending test using five different electrode thicknesses, 133nm, 250nm, 400nm, 533nm and 667nm. The resulting current curves are shown in Figure 4-10. We find that as the electrode thickness increases, the amount of time it takes for the current peak to decay (peak width) increases. In other words, the duration of current increases with electrode thickness.

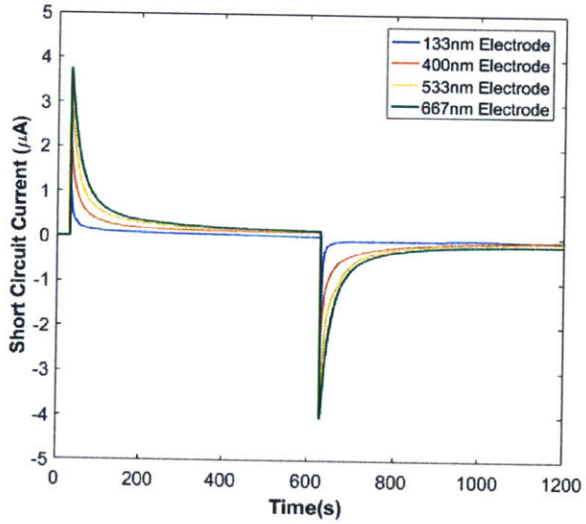

Figure 4-10: Short circuit current during 600 second bending test for 133nm, 400nm, 533nm and 667nm $Li_{3.1}Si$ electrodes. A representative peak for bending and unbending current peaks are shown.

The dimensional analysis for equation (4.3.3) gives a relation that dimension-less diffusion time scales with the square of dimension-less distance. In other words, if the electrode thickness doubles, the anticipated duration of electric current quadruples. The parameter d^2/τ according to electrode thickness is plotted in Figure 4-11a. Here, the electrode thickness is used for the characteristic diffusion length d and peak width for the characteristic diffusion time (τ). As we observe in Figure 4-11a, we find constant d^2/τ for electrodes thicker than 400nm. The constant value of d^2/τ is expected to be an indicator for constant diffusion constant in the electrode material. Not only does this validate the diffusion limited kinetics behavior in electric current generation,

this also suggests the possibility of using this device to measure the lithium diffusivity inside electrochemically active alloy materials.

The irregularity observed for 133nm and 250nm electrodes arise because of the thick electrolyte layer. In the device design, the electrolyte layer is 25μm, approximately two orders of magnitude greater than those of electrodes. With estimated $D = 2.6 \times 10^{-6}\text{cm}^2/s$, the estimated time for a lithium ion to diffuse across the entire thickness of the electrolyte layer is approximately 2.5 seconds. As the electrode gets progressively thinner, the current peak width gets dominated more and more by the electrolyte diffusion. The behavior of d^2/τ will then scale with d^2 alone, with the interpolated y-intercept eventually indicating the diffusion time for electrolyte diffusion until it reaches saturation with electrode-diffusion limited behavior. This explains the irregularity for the electrolyte diffusion limits the current duration.

In chapter 3-3, we have also shown that the equilibrium amount of lithium transfer (equivalently the charge transfer amount) is proportional to the number of lithium present in the electrode (or equivalently total volume of electrodes). Assuming thin film electrodes, the experimentally measured total charge transfer amount for 600seconds and plotted the results in Figure 4-11b. The linear trend between the charge transfer amount and electrode thickness is observed experimentally.

4.4 Conclusion

In this chapter, we examined the kinetic processes present in the device during operation. Among the electrode diffusion, electrolyte diffusion and charge transfer reaction, lithium diffusion inside the electrode was determined to be the rate limiting step for the overall kinetics. By comparing the experimental observation with the numerically solved 1 dimensional model, we explained the the power-law behavior in short circuit current and ratcheting behavior in open circuit voltage measurement. The analysis in this chapter lays the foundation for kinetically optimizing the electrodes when an energy harvester targets a specific frequency motion.

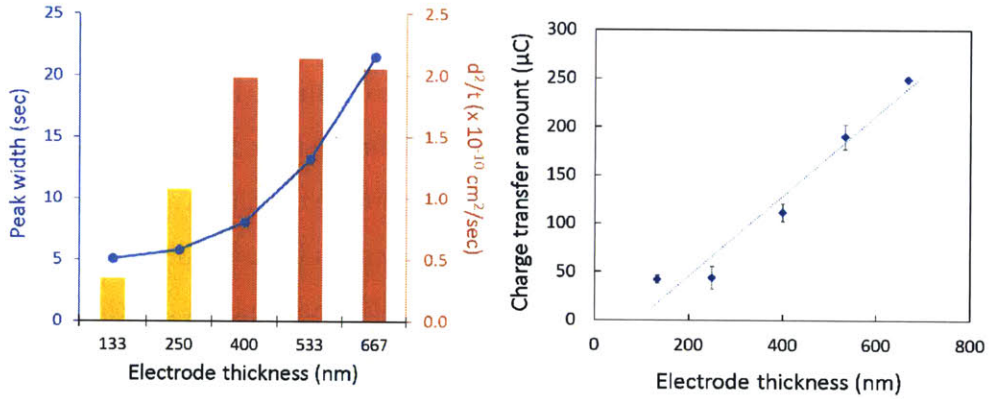

(a) (b)

Figure 4-11: (a) The average current peak width (time it takes for peak current to half) and d^2/τ according to electrode thickness. We find that the peak width increases monotonically with electrode thickness. d^2/τ reaches constant from approximately 400nm electrode thickness. This value is a representation of the diffusion constant, validating the diffusion limited behavior. The low d^2/τ values for 133 and 250nm electrodes suggest overestimated peak width values. This arises from the finite amount of time it takes for Li ion to diffuse across electrolyte layer and is electrolyte diffusion limited. The anticipated behavior of $1/\tau$ is observed. (b) The amount of total charge transfer for 600seconds according to electrode thickness. We observe a linear relationship between the two variables, as expected from mechanics analysis in chapter 3. This indicates that the total amount of electricity generation scales with electrode thickness.

Chapter 5

Device design principles

In this chapter, we will establish the electrode design principles, based on the thermodynamic, mechanics and kinetics analysis presented in Chapter 3 and 4. We will introduce design strategies to maximize the energy output and to target harvesting specific frequency motion. The design principles introduced in this chapter assumes the device design and geometry introduced in chapter 3. Further optimization in the device design will be mentioned briefly in chapter 7, along with other directions for future work.

5.1 Electrode design principles based on thermodynamic and mechanics analysis

The total amount of electrical energy generated by the energy harvester is the product of potential difference and total number of lithium transported.

$$W_{\text{electrical}} \equiv \int V(q)dq = \int \mu_{\text{Li}}(N_{\text{Li}})dN_{\text{Li}} \tag{5.1.1}$$

Thermodynamic and mechanics analysis in chapter 3 introduce insights regarding the voltage output and the expected number of lithium transport at given radii of curvature and stress level. The output voltage is essentially the product of hydrostatic

stress and partial molar volume of lithium.

$$\Delta\mu_{\text{Li}} = eV_{\text{measured}} = \Omega_{\text{Li}}\Delta\sigma_{\text{hydro}} = \Omega_{\text{Li}}\left(\frac{E}{1-\nu}\frac{2h}{3R}\right) \tag{5.1.2}$$

The notations are identical to those used in chapter 3; Ω_{Li}, E, ν, h and R indicate partial molar volume of lithium, Young's modulus of electrode material, Poisson's ratio of electrode material, half the thickness of the device and radius of curvature, respectively. This expression leads us to several important realizations. First, the output potential is directly proportional to Young's modulus. High young's modulus leads to high stress state at a given amount of strain ($1/R$) and leads to higher potential. Noting that the voltage output is limited by the yield strength of the electrode material, using a stronger material increases the maximum voltage the device can generate. This holds true especially because the geometric factors (R, h) may be tuned to set the maximum amount of stress applied to the electrode materials.

Also, using a larger ion than lithium increases voltage output. The partial molar volume, $\Omega_{\text{Li}} \equiv \left(\frac{\partial V}{\partial N_{\text{Li}}}\right)_{P,T,N_{i\neq\text{Li}}}$, directly couples the output voltage and hydrostatic stress difference. Larger sized ions including sodium ion (116pm) or potassium ion (152pm) may increase voltage output from up to 28% and 69% respectively, at the same hydrostatic stress difference. Considering that both sodium and potassium compounds are more common and widely available than lithium compounds, this opens up a possibility for increasing the potential.

Nevertheless, the use of large ions also indicates that the number of atoms needed to relax the applied stress decreases. Mechanics analysis in section 3.3 leads to the following expression for the equilibrium number of atoms needed to fully relax the given stress.

$$\Delta N_{\text{Li}} = \frac{V_{\text{one-side}}}{\Omega_{\text{Li}}}\frac{Tr(\sigma)}{3B} = \frac{V_{\text{one-side}}}{\Omega_{\text{Li}}}\left(\frac{1-2\nu}{1-\nu}\right)\left(\frac{h}{R}\right) \tag{5.1.3}$$

Equation 5.1.3 tells us that the total amount of charge generation is directly proportional to the number of lithium inside the electrode ($\frac{V_{\text{one-side}}}{\Omega_{\text{Li}}}$). In other words, the use of larger ions decreases the atomic density inside the electrode material, leading to smaller current output.

The factor ($\frac{V_{\text{one-side}}}{\Omega_{\text{Li}}}$) also implies that the total charge output is directly proportional to the atomic density of diffusing species. It is desired to use lithium rich material as the electrode choice. For example, Li_3Si is preferred to Li_2Si or $LiCoO_2$ in terms of the total charge generated.

This naturally leads to high capacity anode materials used in secondary batteries as the potential electrode candidates, including Li_xSi, Li_xGe or Na_xSn. Nevertheless, unlike in the battery electrode materials, the total amount of lithium extraction and insertion during the energy harvester operation is very small compared to that during battery operation. Thus, many alloys that were excluded as battery electrodes can be excellent potential electrodes for this type of energy harvester. The candidate materials include any lithium binary alloy with high lithium content such as aluminum-lithium alloy, gallium-lithium alloy or lithium-phosphorous alloy.[57] The large amount of candidates available bring exciting opportunities for further optimization of this device in terms of the materials selection.

In addition, lithium transfer amount directly scales with the volume of electrode affected by stress, suggesting the size scalability of this device. This was experimentally shown in chapter 4 where thin electrodes with different thicknesses varied from 133nm, 250nm, 400nm, 533nm and 667nm exhibited the amount of total charge transfer approximately in ratio of the thickness. (re-write this) While the change in concentration (Δc) is rather small compared to the total concentration (c).

5.2 Design principles based on kinetics analysis

The average power output of an energy harvester depends on the frequency of mechanical input. It is desired that the energy generation timescale matches that of mechanical input. Figure 5-1 illustrates this with a diagram. A naturally occurring mechanical motions may have a continuous, repetitive stress input with frequency f where the stress input lasts for 1/f seconds, stops for another 1/f seconds and repeats this cycle. For instance, human walking is known to be approximately 1-2Hz process. An ideal energy harvester for this motion would generate maximum amount

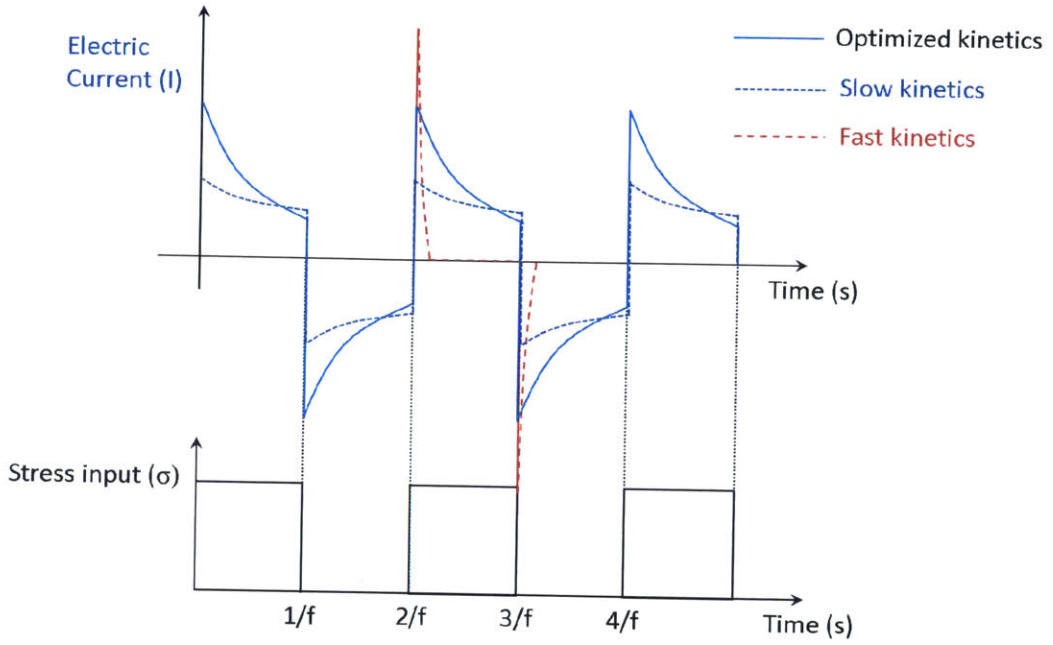

Figure 5-1: Three possible kinetics scenarios of an energy harvester with a repetitive mechanical stress input. f indicates the natural frequency of the stress cycle. The optimized kinetics case, slow kinetics case and fast kinetics cases are illustrated in blue, navy and red, respectively.

of electrical energy for 1 second while the mechanical input lasts. Any continuous energy generation capability over 1 second is not properly utilized or is wasted. With typical current output for our energy harvester, we can think of three possible kinetics scenarios with identical stress input.

In the fast kinetics scenario, the case for many piezoelectric and triboelectric generators, the timescale for energy generation is much faster than that of mechanical input that average power over a stress cycle is low. In slow kinetics scenario, continuous power output is generated, however, its capability to generate longer current output is not utilized. An energy harvester made with thick, dense electrodes would belong to this scenario. We seek to optimize the kinetics such that the area under the curve during the mechanical input is maximized.

$$Q_{\text{generated}} = \Delta N_{\text{Li}} = \int_0^{\tau} I(t)dt = \int_0^{\tau} \frac{\partial c}{\partial t} dt \tag{5.2.1}$$

It is noted that the negative current during rest period (between 1/f and 2/f in Figure 5-1) can be utilized via the use of rectifiers.

In Chapter 4, we showed that the timescale in our energy harvester is limited by lithium diffusion inside electrode. The duration of current output was determined by the electrode thickness, varied between 130nm and 530nm. Based on these results, we established a relationship between dimensionless diffusion distance (d) and dimensionless time (τ). We demonstrated that the relation is followed for sufficiently thick electrodes (thickness than 400nm and 530nm electrodes), given that the kinetics is electrode-diffusion limited.

$$\frac{d^2}{\tau} = \text{constant} \tag{5.2.2}$$

For instance, if the target frequency is 0.1Hz, the desired diffusion distance is approximately 447nm.

It is noted here that the shape of mechanical input also affects the overall efficiency. We derived an expression for the dissipation rate of kinetic processes in Section 2.2.3. The dissipation rate scales with the dot product of flux and the gradient of the conjugate intensive parameter. For our device, the dissipation rate scales with the flux of lithium and the gradient of hydrostatic stress. Noting that the flux of lithium is proportional to the gradient of stress (essentially the driving force for flux), the dissipation rate scales with the square of the hydrostatic stress gradient. When given a square wave of mechanical stress input as shown in Figure 5-1, the stress input involves the summation of high frequency modes in Fourier transform. These high frequency modes essentially involves increased dissipation rate (increased entropy production) and decreases the overall efficiency. If a slowly varied, single frequency wave of stress input is applied, increased overall efficiency will be observed experimentally compared to that calculated in Section 3.4.3. This is in parallel with the notion of quasistatic process and reversible thermodynamics. Any rapidly varying physical process will involve entropy production and reduced efficiency compared to the thermodynamically achievable efficiency via slowly varying, quasistatic process.

5.3 Conclusions

Based on these findings in this chapter, we can argue that designing an ideal electrode for specific frequency motion is a constrained optimization problem. On one hand, since the total amount of charge transfer scales with the volume of electrode, we would like to increase the electrode volume. On the other hand, thick electrodes result in long diffusion distance and we may not be able to utilize the energy generation capability within the stress duration. Instead, it is desired to enhance kinetic properties by introducing porosity, in order to decrease electrode diffusion distance and increase the surface area for charge transfer reaction. The kinetics of electrolyte diffusion may also need to be considered when targeting high frequency motion. This also suggests the guidelines for tuning diffusion lengths for all solid electrode-electrolyte composite based energy harvester.

Chapter 6

Concluding remarks

In this thesis, we introduced our work on electrochemically driven mechanical energy harvester, a novel type of energy harvester based on electrochemical principles. With the rising interest on energy sustainability and internet of things devices, interest in more efficient energy harvesters is growing. Also, this device demonstrates the first applicable use of a scientifically interesting property, stress-composition coupling in electrochemical alloys. Until now, this property has often been considered adverse in applications such as secondary batteries.

We began by developing the thermodynamic grounds for harvesting bending-unbending cycles with electrochemical alloys (Chapter 3). The thermodynamic cycle similar in spirit to Carnot cycle was developed. The mechanics analysis of stress states inside the electrodes provided grounds for device design and experimental verification of the grounding thermodynamic concepts.

Analysis on timescale tunability of this device followed in Chapter 4. By analyzing the kinetic processes inside the device, we demonstrated by modeling and experiments that the duration of electric current generated by this device is dominated by lithium diffusion inside the electrode material. This tunability in the duration of electric current was first demonstrated in this work, among all other types of mechanical energy harvesters.

The relevant design principles, based on the works in Chapter 3 and 4, were presented in Chapter 5. In order to maximize the voltage output, electrode materi-

als with high Young's modulus provides high voltage output. Electrodes with large atomic density of diffusing species increase the current output. Also, the duration of current scales with the square of diffusion distance. Based on these principles, we argued that designing an electrode for targeted frequency motion involves constrained optimization problem between energy density and power. The presented design principles provide guidelines for porous electrode design.

Based on analyses presented in the thesis, we can summarize several unique characteristics of this device compared to conventional mechanical energy harvesters. The main strengths of this device includes the following.

Size scalability The device generates continuous electric current in a scalable manner. The amount of current generated is proportional to the volume of electrodes and the mechanical stress applied to the electrode. (Section 3.3) The electrodes can, therefore, be prepared in variable sizes to meet specific application needs and energy output. This size scalability arises uniquely from the working principle of our device, wherein mechanically stressed Li_xSi adjusts its composition according to the stress-potential coupling. In addition, the continuous, tunable duration of electric current generated by our device yields quite high energy output per motion. (Section 3.5) In contrast, MEMS/NEMS or electrostatic motion based harvesters feature short duration of current output (on the order of 10-100msec) and are efficient on harvesting motions with vibrational frequency over 20Hz. While the use of clamped resonators or springs transforms low frequency motions into vibrations of the resonators, it constrains the geometry and size of the devices.[33, 34] This makes resonators or cantilevers in MEMS/NEMS devices difficult to scale in size.

Geometry flexibility Our device can also be prepared in any geometry. The only geometric requirement based on the electrochemical working principle is three-layer (electrode-electrolyte-electrode) assembly. There is no need for a cantilever or a vibrator, which are often required in electrostatic or magnetic induction generators.[74, 75] In this thesis, we have demonstrated a thin-film based prototype with bending mechanical input.(Section 3.2) As long as a spatially asymmetric stress field can be applied to the two electrodes, the device is capable of generating electricity with any

shape and size. This geometric flexibility provides wide applicability. For instance, a similar device prototype can be used to harvest the energy generated by human walking, wherein one electrode is subjected to compressive stress due to human weight, while the other is stress free.

Low internal resistance Internal resistance is a measure of energy dissipation when the generated electricity powers the external loads, an important index characterizing energy utilization efficiency of a device. Since the device is built upon electrochemical reactions, its internal resistance is similar to that of secondary batteries, significantly lower than that of its competitors such as piezoelectric or triboelectric generators. The electrode materials for these generators generally consist of insulating materials such as perovskite ceramics or polymers and the internal resistance of these devices can be as high as 100MΩ.[62] In comparison, preliminary data on our device demonstrates that the internal resistance is estimated to be only 300Ω, several orders of magnitudes smaller than typical piezoelectric generators. (Section 3.4)

Manufacturing base The fabrication of this device utilizes much of the same tools and processes developed for lithium ion battery industry. The scaled-up process has been well established, including slurry processing and roll-to-roll electrode coating, that are fully automated and quality controlled. The scaled-up fabrication of this kind of harvester is, thus, expected to be straightforward and cost-effective, leveraging the existing industrial infrastructure.

Nontoxicity Finally, the method utilizes non-toxic, earth abundant materials. Often, successful piezoelectric devices contain certain amount of lead in its perovskite ceramic. The toxicity of lead has been constantly raised and restriction of hazardous substance directive (RoHS) discourages the use of lead in wide applications, especially for wearable devices.[35]

Chapter 7

Directions for future work

The work and analysis demonstrated in this thesis brings design guidelines for specifically targeted motion harvesting and scientifically interesting questions to pursue.

By demonstrating the current duration tunability, we suggested the design of porous electrode. The design is based on the premise to control the diffusion distance of lithium inside the electrode. Also, the pores are expected to be filled completely with electrolyte to ensure large surface area for charge transfer kinetics. The design and fabrication of such electrode remains to be performed. Several fabrication methods have been demonstrated for porous electrode design, including the use of nanoscale 3D printer[76] and the use of colloidal templated growth.[77] The mechanics of such electrodes during bending involves complications including stress concentration factor which remain to be answered as well.

Another rational electrode design may utilize the electrode-electrolyte composite, often employed in solid oxide fuel cell electrodes.[78] Fast lithium or sodium conductors have been demonstrated as solid state electrolytes in various systems, and enrich the design space for the device in solid state.[79, 80] The diffusion distance inside electrolyte as well as electrode are expected to be tunable.

While this thesis focused on the application of stress-potential coupling as an energy harvester, this may be utilized in other scientifically exciting applications. One such application involves the measurement of diffusivity. While operating in the elastic regime, the device introduces a small perturbation in alloy composition between

two originally identical electrodes. By allowing the two electrodes to equilibrate over time, we may deduce the kinetic properties inside the system such as diffusivity. Since the method does not involve any heat treatment, the kinetic properties of specific microstructured alloy or specific composition alloy can be performed. Also, considering that this can be employed for any electrochemical system with relevant electrolyte, the method may be extended as a general method.

Another application involves the identification of viscoelastic properties of electrode materials. Traditionally, viscoelastic properties are measured via directly applying stress or strain to the material and measuring the strain or stress response over time. Such method is limited in terms of its applicability, since some technologically relevant electrochemical alloys are either sensitive to air, difficult to prepare in bulk specimen or challenging to track time dependent stress or strain. One such measurement was performed via in situ measurement inside a TEM, nevertheless, was difficult to generalize in terms of shape and size.[81] Keeping in mind that the device allows us to monitor/control the strain via radius of curvature, stress via potential measurement, stress relaxation via electric current and strain rate via bending speed, we have relevant handles for viscoelastic measurements.

Noting that the device utilizes induced cathodes and anodes via introducing externally applied stimuli, we may develop other kinds of energy harvesters based on this principle. For instance, a thermal energy harvester may be developed based on the same principle and analysis framework.

Bibliography

[1] Steven R Anton and Henry A Sodano. A review of power harvesting using piezoelectric materials (2003–2006). *Smart Materials and Structures*, 16(3):R1–R21, June 2007.

[2] Ming-Chang Lu, Srinath Satyanarayana, Rohit Karnik, Arun Majumdar, and Chi-Chuan Wang. A mechanical-electrokinetic battery using a nano-porous membrane. *Journal of Micromechanics and Microengineering*, 16(4):667–675, April 2006.

[3] Feng-Ru Fan, Zhong-Qun Tian, and Zhong Lin Wang. Flexible triboelectric generator. *Nano Energy*, 1(2):328–334, March 2012.

[4] Rickard Armiento, Boris Kozinsky, Marco Fornari, and Gerbrand Ceder. Screening for high-performance piezoelectrics using high-throughput density functional theory. *Physical Review B*, 84(1), July 2011.

[5] Frank H. J. van der Heyden, Douwe Jan Bonthuis, Derek Stein, Christine Meyer, and Cees Dekker. Power Generation by Pressure-Driven Transport of Ions in Nanofluidic Channels. *Nano Letters*, 7(4):1022–1025, April 2007.

[6] Jong Kyun Moon, Jaeki Jeong, Dongyun Lee, and Hyuk Kyu Pak. Electrical power generation by mechanically modulating electrical double layers. *Nature Communications*, 4:1487, February 2013.

[7] G. L. Messing, S. Trolier-McKinstry, E. M. Sabolsky, C. Duran, S. Kwon, B. Brahmaroutu, P. Park, H. Yilmaz, P. W. Rehrig, K. B. Eitel, E. Suvaci, M. Seabaugh, and K. S. Oh. Templated Grain Growth of Textured Piezoelectric Ceramics. *Critical Reviews in Solid State and Materials Sciences*, 29(2):45–96, April 2004.

[8] Geon-Tae Hwang, Hyewon Park, Jeong-Ho Lee, SeKwon Oh, Kwi-Il Park, Myunghwan Byun, Hyelim Park, Gun Ahn, Chang Kyu Jeong, Kwangsoo No, HyukSang Kwon, Sang-Goo Lee, Boyoung Joung, and Keon Jae Lee. Self-Powered Cardiac Pacemaker Enabled by Flexible Single Crystalline PMN-PT Piezoelectric Energy Harvester. *Advanced Materials*, 26(28):4880–4887, July 2014.

[9] Chang Bao Han, Weiming Du, Chi Zhang, Wei Tang, Limin Zhang, and Zhong Lin Wang. Harvesting energy from automobile brake in contact and non-contact mode by conjunction of triboelectrication and electrostatic-induction processes. *Nano Energy*, 6:59–65, May 2014.

[10] Xiangyu Chen, Mitsumasa Iwamoto, Zhemin Shi, Limin Zhang, and Zhong Lin Wang. Self-Powered Trace Memorization by Conjunction of Contact-Electrification and Ferroelectricity. *Advanced Functional Materials*, 25(5):739–747, February 2015.

[11] Sihong Wang, Yannan Xie, Simiao Niu, Long Lin, and Zhong Lin Wang. Free-standing Triboelectric-Layer-Based Nanogenerators for Harvesting Energy from a Moving Object or Human Motion in Contact and Non-contact Modes. *Advanced Materials*, 26(18):2818–2824, May 2014.

[12] Simiao Niu, Xiaofeng Wang, Fang Yi, Yu Sheng Zhou, and Zhong Lin Wang. A universal self-charging system driven by random biomechanical energy for sustainable operation of mobile electronics. *Nature Communications*, 6:8975, December 2015.

[13] Yihua Liu, Dincer Gokcen, Ugo Bertocci, and Thomas Moffat. Self-Terminating Growth of Platinum Films by Electrochemical Deposition. *Science*, 338(6112):1328–1330, December 2012.

[14] Dongchan Jang, Xiaoyan Li, Huajian Gao, and Julia R. Greer. Deformation mechanisms in nanotwinned metal nanopillars. *Nature Nanotechnology*, 7(9):594–601, July 2012.

[15] Run Liu, Alexey A. Vertegel, Eric W. Bohannan, Thomas A. Sorenson, and Jay A. Switzer. Epitaxial Electrodeposition of Zinc Oxide Nanopillars on Single-Crystal Gold. *Chemistry of Materials*, 13(2):508–512, 2001.

[16] M. N. Obrovac and Leif Christensen. Structural Changes in Silicon Anodes during Lithium Insertion/Extraction. *Electrochemical and Solid-State Letters*, 7(5):A93, 2004.

[17] Wei-Jun Zhang. A review of the electrochemical performance of alloy anodes for lithium-ion batteries. *Journal of Power Sources*, 196(1):13–24, January 2011.

[18] Xin Su, Qingliu Wu, Juchuan Li, Xingcheng Xiao, Amber Lott, Wenquan Lu, Brian W. Sheldon, and Ji Wu. Silicon-Based Nanomaterials for Lithium-Ion Batteries: A Review. *Advanced Energy Materials*, 4(1):n/a–n/a, January 2014.

[19] Tadhg Kennedy, Emma Mullane, Hugh Geaney, Michal Osiak, Colm O'Dwyer, and Kevin M. Ryan. High-Performance Germanium Nanowire-Based Lithium-Ion Battery Anodes Extending over 1000 Cycles Through in Situ Formation of a Continuous Porous Network. *Nano Letters*, 14(2):716–723, 2014.

[20] Candace K. Chan, Hailin Peng, Gao Liu, Kevin McIlwrath, Xiao Feng Zhang, Robert A. Huggins, and Yi Cui. High-performance lithium battery anodes using silicon nanowires. *Nature Nanotechnology*, 3(1):31–35, January 2008.

[21] Kejie Zhao, Wei L. Wang, John Gregoire, Matt Pharr, Zhigang Suo, Joost J. Vlassak, and Efthimios Kaxiras. Lithium-Assisted Plastic Deformation of Silicon Electrodes in Lithium-Ion Batteries: A First-Principles Theoretical Study. *Nano Letters*, 11(7):2962–2967, July 2011.

[22] Sumit K. Soni, Brian W. Sheldon, Xingcheng Xiao, Allan F. Bower, and Mark W. Verbrugge. Diffusion mediated lithiation stresses in Si thin film electrodes. *Journal of The Electrochemical Society*, 159(9):A1520–A1527, 2012.

[23] Sumit K. Soni, Brian W. Sheldon, Xingcheng Xiao, and Anton Tokranov. Thickness effects on the lithiation of amorphous silicon thin films. *Scripta Materialia*, 64(4):307–310, February 2011.

[24] Hui Yang, Shan Huang, Xu Huang, Feifei Fan, Wentao Liang, Xiao Hua Liu, Long-Qing Chen, Jian Yu Huang, Ju Li, Ting Zhu, and Sulin Zhang. Orientation-Dependent Interfacial Mobility Governs the Anisotropic Swelling in Lithiated Silicon Nanowires. *Nano Letters*, 12(4):1953–1958, April 2012.

[25] Meng Gu, Hui Yang, Daniel E. Perea, Ji-Guang Zhang, Sulin Zhang, and Chong-Min Wang. Bending-Induced Symmetry Breaking of Lithiation in Germanium Nanowires. *Nano Letters*, 14(8):4622–4627, August 2014.

[26] Jiang Wei Wang, Yu He, Feifei Fan, Xiao Hua Liu, Shuman Xia, Yang Liu, C. Thomas Harris, Hong Li, Jian Yu Huang, Scott X. Mao, and Ting Zhu. Two-Phase Electrochemical Lithiation in Amorphous Silicon. *Nano Letters*, 13(2):709–715, February 2013.

[27] Xiao Hua Liu, Feifei Fan, Hui Yang, Sulin Zhang, Jian Yu Huang, and Ting Zhu. Self-Limiting Lithiation in Silicon Nanowires. *ACS Nano*, 7(2):1495–1503, February 2013.

[28] Xiao Hua Liu, He Zheng, Li Zhong, Shan Huang, Khim Karki, Li Qiang Zhang, Yang Liu, Akihiro Kushima, Wen Tao Liang, Jiang Wei Wang, Jeong-Hyun Cho, Eric Epstein, Shadi A. Dayeh, S. Tom Picraux, Ting Zhu, Ju Li, John P. Sullivan, John Cumings, Chunsheng Wang, Scott X. Mao, Zhi Zhen Ye, Sulin Zhang, and Jian Yu Huang. Anisotropic Swelling and Fracture of Silicon Nanowires during Lithiation. *Nano Letters*, 11(8):3312–3318, August 2011.

[29] Xiao Hua Liu, Li Zhong, Shan Huang, Scott X. Mao, Ting Zhu, and Jian Yu Huang. Size-Dependent Fracture of Silicon Nanoparticles During Lithiation. *ACS Nano*, 6(2):1522–1531, February 2012.

[30] Wentao Liang, Hui Yang, Feifei Fan, Yang Liu, Xiao Hua Liu, Jian Yu Huang, Ting Zhu, and Sulin Zhang. Tough Germanium Nanoparticles under Electrochemical Cycling. *ACS Nano*, 7(4):3427–3433, April 2013.

[31] F. R. N. Nabarro. Steady-state diffusional creep. *Philosophical Magazine*, 16(140):231–237, August 1967.

[32] Davion Hill, Arun Agarwal, and Nellie Tong. Assessment of Piezoelectric Materials for Roadway Energy Harvesting: Cost of Energy and Demonstration Roadmap, January 2014.

[33] Arman Hajati and Sang-Gook Kim. Ultra-wide bandwidth piezoelectric energy harvesting. *Applied Physics Letters*, 99(8):083105, 2011.

[34] Evan Baker, Timothy Reissman, Fan Zhou, Chen Wang, Kevin Lynch, and Cheng Sun. Microstereolithography of Three-Dimensional Polymeric Springs for Vibration Energy Harvesting. *Smart Materials Research*, 2012:1–9, 2012.

[35] E. U. Parliament and E. U. Council. Directive 2002/95/EC on the restriction of the use of certain hazardous substances in electrical and electronic equipment. *Official J Eur Union*, 46:19–23, 2003.

[36] E Gurtin, E Fried, and Lallit Anand. *The Mechanics And Thermodynamics Of Continua*. Cambridge University Press, 2010.

[37] Wallace Duane. *Thermodynamics of Crystals*. John Wiley & Sons, Inc., 1972.

[38] Robert W Balluffi, Samuel M Allen, and W. Craig Carter. *Kinetics of Materials*. John Wiley & Sons, Inc., 2005.

[39] Byoung-Yong Chang and Su-Moon Park. Electrochemical Impedance Spectroscopy. *Annual Review of Analytical Chemistry*, 3(1):207–229, June 2010.

[40] Nanshu Lu, Xi Wang, Zhigang Suo, and Joost Vlassak. Failure by simultaneous grain growth, strain localization, and interface debonding in metal films on polymer substrates. *Journal of Materials Research*, 24(02):379–385, February 2009.

[41] Yueh-Lin Loo, Robert L. Willett, Kirk W. Baldwin, and John A. Rogers. Interfacial Chemistries for Nanoscale Transfer Printing. *Journal of the American Chemical Society*, 124(26):7654–7655, July 2002.

[42] Gi-Dong Sim, Sejeong Won, and Soon-Bok Lee. Tensile and fatigue behaviors of printed Ag thin films on flexible substrates. *Applied Physics Letters*, 101(19):191907, 2012.

[43] Gi-Dong Sim, Yun Hwangbo, Hyun-Ho Kim, Soon-Bok Lee, and Joost J. Vlassak. Fatigue of polymer-supported Ag thin films. *Scripta Materialia*, 66(11):915–918, June 2012.

[44] Oliver Graudejus, Patrick Görrn, and Sigurd Wagner. Controlling the Morphology of Gold Films on Poly(dimethylsiloxane). *ACS Applied Materials & Interfaces*, 2(7):1927–1933, 2010.

[45] F. Faupel, C. H. Yang, S. T. Chen, and P. S. Ho. Adhesion and deformation of metal/polyimide layered structures. *Journal of Applied Physics*, 65(5):1911, 1989.

[46] Won Mook Choi, Jizhou Song, Dahl-Young Khang, Hanqing Jiang, Yonggang Y. Huang, and John A. Rogers. Biaxially Stretchable "Wavy" Silicon Nanomembranes. *Nano Letters*, 7(6):1655–1663, June 2007.

[47] John A. Rogers, Takao Someya, and Yonggang Huang. Materials and mechanics for stretchable electronics. *Science*, 327(5973):1603–1607, 2010.

[48] Gi-Dong Sim, Sejeong Won, Chun-yan Jin, Inkyu Park, Soon-Bok Lee, and Joost J. Vlassak. Improving the stretchability of as-deposited Ag coatings on poly-ethylene-terephthalate substrates through use of an acrylic primer. *Journal of Applied Physics*, 109(7):073511, 2011.

[49] Brian W. Sheldon, Sumit K. Soni, Xingcheng Xiao, and Yue Qi. Stress contributions to solution thermodynamics in Li-Si alloys. *Electrochemical and Solid-State Letters*, 15(1):A9–A11, 2011.

[50] Hui Yang, Wentao Liang, Xu Guo, Chong-Min Wang, and Sulin Zhang. Strong kinetics-stress coupling in lithiation of Si and Ge anodes. *Extreme Mechanics Letters*, 2:1–6, March 2015.

[51] Kai He, Huolin L. Xin, Kejie Zhao, Xiqian Yu, Dennis Nordlund, Tsu-Chien Weng, Jing Li, Yi Jiang, Christopher A. Cadigan, Ryan M. Richards, Marca M. Doeff, Xiao-Qing Yang, Eric A. Stach, Ju Li, Feng Lin, and Dong Su. Transitions from Near-Surface to Interior Redox upon Lithiation in Conversion Electrode Materials. *Nano Letters*, 15(2):1437–1444, February 2015.

[52] V. A. Sethuraman, V. Srinivasan, A. F. Bower, and P. R. Guduru. In Situ Measurements of Stress-Potential Coupling in Lithiated Silicon. *Journal of The Electrochemical Society*, 157(11):A1253, 2010.

[53] M. N. Obrovac, Leif Christensen, Dinh Ba Le, and J. R. Dahn. Alloy Design for Lithium-Ion Battery Anodes. *Journal of The Electrochemical Society*, 154(9):A849, 2007.

[54] V. L. Chevrier and J. R. Dahn. First Principles Model of Amorphous Silicon Lithiation. *Journal of The Electrochemical Society*, 156(6):A454, 2009.

[55] Shigeki Ohara, Junji Suzuki, Kyoichi Sekine, and Tsutomu Takamura. A thin film silicon anode for Li-ion batteries having a very large specific capacity and long cycle life. *Journal of Power Sources*, 136(2):303–306, October 2004.

[56] John Cannarella, Xinyi Liu, Collen Z. Leng, Patrick D. Sinko, Gennady Y. Gor, and Craig B. Arnold. Mechanical Properties of a Battery Separator under Compression and Tension. *Journal of The Electrochemical Society*, 161(11):F3117–F3122, 2014.

[57] Naoki Nitta and Gleb Yushin. High-Capacity Anode Materials for Lithium-Ion Batteries: Choice of Elements and Structures for Active Particles. *Particle & Particle Systems Characterization*, 31(3):317–336, March 2014.

[58] Kangning Ren, Yihua Zhao, Jing Su, Declan Ryan, and Hongkai Wu. Convenient Method for Modifying Poly(dimethylsiloxane) To Be Airtight and Resistive against Absorption of Small Molecules. *Analytical Chemistry*, 82(14):5965–5971, July 2010.

[59] Kejie Zhao, Georgios A. Tritsaris, Matt Pharr, Wei L. Wang, Onyekwelu Okeke, Zhigang Suo, Joost J. Vlassak, and Efthimios Kaxiras. Reactive Flow in Silicon Electrodes Assisted by the Insertion of Lithium. *Nano Letters*, 12(8):4397–4403, August 2012.

[60] V.B. Shenoy, P. Johari, and Y. Qi. Elastic softening of amorphous and crystalline Li–Si Phases with increasing Li concentration: A first-principles study. *Journal of Power Sources*, 195(19):6825–6830, October 2010.

[61] Benjamin Hertzberg, Jim Benson, and Gleb Yushin. Ex-situ depth-sensing indentation measurements of electrochemically produced Si–Li alloy films. *Electrochemistry Communications*, 13(8):818–821, August 2011.

[62] Kwi-Il Park, Jung Hwan Son, Geon-Tae Hwang, Chang Kyu Jeong, Jungho Ryu, Min Koo, Insung Choi, Seung Hyun Lee, Myunghwan Byun, Zhong Lin Wang, and Keon Jae Lee. Highly-Efficient, Flexible Piezoelectric PZT Thin Film Nanogenerator on Plastic Substrates. *Advanced Materials*, 26(16):2514–2520, April 2014.

[63] Sangtae Kim, Soon Ju Choi, Kejie Zhao, Hui Yang, Giorgia Gobbi, Sulin Zhang, and Ju Li. Electrochemically driven mechanical energy harvesting. *Nature Communications*, 7:10146, January 2016.

[64] Kwi-Il Park, Minbaek Lee, Ying Liu, San Moon, Geon-Tae Hwang, Guang Zhu, Ji Eun Kim, Sang Ouk Kim, Do Kyung Kim, Zhong Lin Wang, and Keon Jae Lee. Flexible Nanocomposite Generator Made of BaTiO3 Nanoparticles and Graphitic Carbons. *Advanced Materials*, 24(22):2999–3004, June 2012.

[65] Youfan Hu, Long Lin, Yan Zhang, and Zhong Lin Wang. Replacing a Battery by a Nanogenerator with 20 V Output. *Advanced Materials*, 24(1):110–114, January 2012.

[66] Chang Kyu Jeong, Kwi-Il Park, Jungho Ryu, Geon-Tae Hwang, and Keon Jae Lee. Large-Area and Flexible Lead-Free Nanocomposite Generator Using Alkaline Niobate Particles and Metal Nanorod Filler. *Advanced Functional Materials*, 24(18):2620–2629, May 2014.

[67] Sang-Gook Kim, Shashank Priya, and Isaku Kanno. Piezoelectric MEMS for energy harvesting. *MRS Bulletin*, 37(11):1039–1050, November 2012.

[68] Feng Ru Fan, Jianjun Luo, Wei Tang, Chaoyu Li, Cuiping Zhang, Zhongqun Tian, and Zhong Lin Wang. Highly transparent and flexible triboelectric nanogenerators: performance improvements and fundamental mechanisms. *Journal of Materials Chemistry A*, 2(33):13219, July 2014.

[69] Giacomo Gafforelli, Alberto Corigliano, Ruize Xu, and Sang-Gook Kim. Experimental verification of a bridge-shaped, nonlinear vibration energy harvester. *Applied Physics Letters*, 105(20):203901, November 2014.

[70] A. Van der Ven, G. Ceder, M. Asta, and P. D. Tepesch. First-principles theory of ionic diffusion with nondilute carriers. *Physical Review B*, 64(18), October 2001.

[71] Thomas Maxisch, Fei Zhou, and Gerbrand Ceder. *Ab initio* study of the migration of small polarons in olivine Li x FePO 4 and their association with lithium ions and vacancies. *Physical Review B*, 73(10), March 2006.

[72] Kang Xu. Nonaqueous Liquid Electrolytes for Lithium-Based Rechargeable Batteries. *Chemical Reviews*, 104(10):4303–4418, 2004.

[73] Kendall A Atkinson. *An Introduction to Numerical Analysis.* John Wiley & Sons, Inc., 2nd edition edition, 1989.

[74] S Boisseau, G Despesse, T Ricart, E Defay, and A Sylvestre. Cantilever-based electret energy harvesters. *Smart Materials and Structures*, 20(10):105013, October 2011.

[75] Loreto Mateu and Francesc Moll. Review of energy harvesting techniques and applications for microelectronics (Keynote Address). *Proc. SPIE*, 5837:359–373, 2005.

[76] M. Hermatschweiler, A. Ledermann, A. Ozin, G. M. Wegener, and G. von Freymann. Fabrication of Silicon Inverse Woodpile Photonic Crystals. *Advanced Functional Materials*, 17(14):2273–2277, September 2007.

[77] Hongwei Yan, Sergey Sokolov, Justin C. Lytle, Andreas Stein, Fan Zhang, and William H. Smyrl. Colloidal-Crystal-Templated Synthesis of Ordered Macroporous Electrode Materials for Lithium Secondary Batteries. *Journal of The Electrochemical Society*, 150(8):A1102, 2003.

[78] Chunwen Sun, Rob Hui, and Justin Roller. Cathode materials for solid oxide fuel cells: a review. *Journal of Solid State Electrochemistry*, 14(7):1125–1144, July 2010.

[79] Noriaki Kamaya, Kenji Homma, Yuichiro Yamakawa, Masaaki Hirayama, Ryoji Kanno, Masao Yonemura, Takashi Kamiyama, Yuki Kato, Shigenori Hama, Koji Kawamoto, and Akio Mitsui. A lithium superionic conductor. *Nature Materials*, 10(9):682–686, July 2011.

[80] William D. Richards, Tomoyuki Tsujimura, Lincoln J. Miara, Yan Wang, Jae Chul Kim, Shyue Ping Ong, Ichiro Uechi, Naoki Suzuki, and Gerbrand Ceder. Design and synthesis of the superionic conductor Na10SnP2S12. *Nature Communications*, 7:11009, March 2016.

[81] Steven T. Boles, Carl V. Thompson, Oliver Kraft, and Reiner Mönig. In situ tensile and creep testing of lithiated silicon nanowires. *Applied Physics Letters*, 103(26):263906, December 2013.